UNIVERSITY OF OKLAHOMA

GRADUATE COLLEGE

MATERIAL AND PHOTONIC ENGINEERING ON LEAD SELENIDE NANOCRYSTAL FILMS FOR MID-INFRARED EMITTER DEVELOPMENT

A THESIS

SUBMITTED TO THE GRADUATE FACULTY

in partial fulfillment of the requirements for the

Degree of

MASTER OF SCIENCE

BY

AHSAN EJAZ
Norman, Oklahoma
2025

MATERIAL AND PHOTONIC ENGINEERING ON LEAD SELENIDE NANOCRYSTAL FILMS FOR MID-INFRARED EMITTER DEVELOPMENT

A THESIS APPROVED FOR THE
SCHOOL OF ELECTRICAL AND COMPUTER ENGINEERING

BY THE COMMITTEE CONSISTING OF

Dr. Binbin Weng, Chair

Dr. Zhisheng Shi, Member

Dr. Hanjong Paik, Member

© Copyright by AHSAN EJAZ 2025
All Rights Reserved.

Acknowledgments

I would like to thank my friends, family, professors and classmates who I have worked with as a graduate student at the University of Oklahoma. Namely, I would like to thank Dr. Binbin Weng for his continued guidance and support in my research and lab work under the Nanophotonics Laboratory in the School of Electrical and Computer Engineering. I would also like to thank Dr. Mark E. Curtis, Dr. Preston R. Larson, and Cleanroom staff Dr. Gang Yang, Dr. Srujana Prayakarao who have been encouraging and resourceful in my experimental research endeavors. Finally, I would like to thank my parents, siblings and specially my wife and daughter for their sacrifices and support in completing my master's degree. Their sacrifice forms the foundation of all that I have accomplished.

Ahsan Ejaz

Table of Contents

List of Figures

List of Tables

Abstract

Lead selenide (PbSe) is a IV-VI semiconductor material and is known to have a high absorption coefficient. This property comes from its narrow band gap (0.27eV) and strong interaction with light within the material. This means that it efficiently absorbs a significant amount of light relative to its thickness. The high absorption coefficient makes it a promising material also for solar cell absorbers, as it efficiently converts light into electrical current over a broad wavelength range. Research on PbSe has been ongoing for nearly a century, with continuous advancements in understanding its properties and potential applications. The full extent of its physical properties remains underutilized in practical devices. Despite significant advancements in recent technologies, there is still considerable potential for improving the performance and cost-efficiency of miniaturized MIR gas sensing systems.

This thesis aims to develop a narrowband mid-infrared emitter by leveraging photonic engineering techniques applied to lead selenide (PbSe) nanocrystals. A key challenge lies in the inherently low radiative efficiency of PbSe, particularly at room temperature, where non-radiative processes, most notably Auger recombination tend to dominate carrier dynamics.

The first chapter of the thesis presents an overview of the properties of Lead Selenide (PbSe) and High Contrast Gratings (HCG) in the context of mid-infrared photodetection. It examines various PbSe growth techniques, emphasizing the relevance of the Chemical Bath Deposition method. Furthermore, it introduces a novel approach known as Oriented Attachment, underscoring its role in improving the material characteristics of PbSe.

Chapter two of the thesis focused on deposition PbSe using Chemical Bath Deposition method, which allow the cost-effective and scalable fabrication of MIR photonic devices. In this study, I employed the water bath method to grow uniform PbSe

nanocrystals using the Oriented Attachment technique on amorphous substrates. Different parameters were varied during the growth process and their effects were critically analysed.

In chapter three, I studied about the annealing effects on PbSe sample. After annealing with nitrogen at different temperatures, photo luminesce significantly improved. Surface morphologies before and after the annealing of PbSe thin films were studied by Scanning Electron Microscope (SEM) and X-Ray Diffraction (XRD).

The chapter four of this thesis explores the nanostructure design simulated using RSoft software, followed by the fabrication methods applied to lead selenide samples which includes the photolithography process. This work contributes to the goal of developing compact, cost-effective, low-power, and highly efficient on-chip MIR narrowband emitter for chemical sensing applications. This work explores methods to enhance PbSe film quality, along with the design and fabrication of photonic structures on PbSe samples, potentially improving the performance of PbSe-based MWIR sensing platforms.

Additionally, the potential future work aimed at enhancing the performance of PbSe emitters and photodetectors will be discussed in the concluding section of the thesis.

CHAPTER 1

Introduction

1.1 Mid-Infrared Lead Salt Semiconductors

The mid-infrared (MIR) wavelength ranging from 2.5 to 20 μm (4000 to 500 cm^{-1}) [4] is regarded as the molecular fingerprint region, as it contains strong and distinguishing fundamental molecular absorption bands as compared to other spectral domains such as the near-infrared (NIR) range. Because of this unique feature, the spectroscopy instruments operating in the MIR range serves as a powerful tool for chemical sensing, material analysis, and biomedical diagnostics. With the development of network technologies, there has been a fast growing interest in advancing the MIR optoelectronic devices for revolutionizing the traditional MIR chemical sensing technologies towards the solutions with much higher-level miniaturization and smartness standards.

In order to advance the optoelectronic devices, a high quality suitable material platform serves as the critical foundation that could play as a determining factor on the eventual device performance. With that said, in the MIR range, there is only a handful choices including the III-V group semiconductors such as indium antimonide (InSb), indium gallium arsenide (InGaAs), II-VI group semiconductors such as HgCdTe, and IV-VI group lead salt semiconductors such as lead teluride (PbTe), lead selenide (PbSe). Among which, IV-VI semiconductor, specially for PbSe, it is regarded as one of the most popular options due to its unique electronic and photonic properties for developing low-cost infrared detection and gas sensing technologies.

Most improtantly, IV-VI semiconductor (e.g., PbSe material), intrinsically, has much lower Auger recombination coefficients than other semiconductor material systems.

As shown in Fig.1.1, Auger coefficient of IV-VI semiconductors is about one to two orders of magnitude lower than II-VI (e.g., HgCdTe) and III-V (e.g., InAs) at room temperature [5], as highlighted in the pink dashed circle.

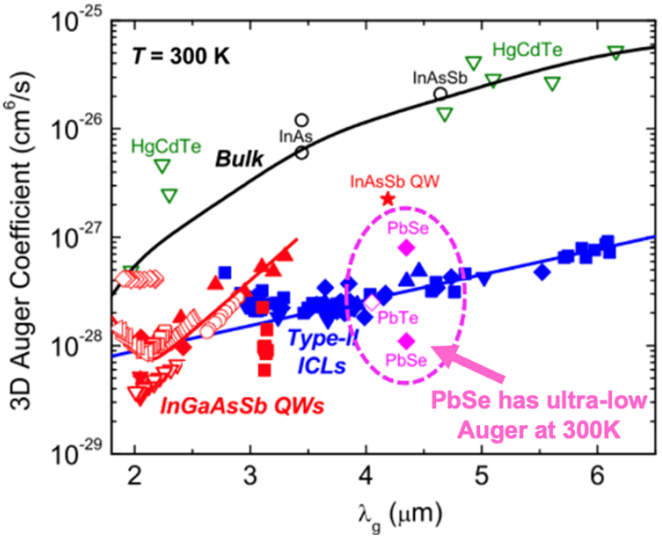

Fig. 1.1: Auger Coefficients Comparison among different materials in the MIR region [1].

Auger coefficient describes the non-radiative recombination process, playing a critical role to impact the material quantum efficiency and thus the optoelectronic devices performance such as light emitters and photodetectors. The mechanism gets more sever and can dominate the recombination at higher temperature, simply due to its triple order relationship with the increasing carrier concentration through this process. Therefore, In MIR optoelectronic devices, high operating temperatures is a challenge for traditional III-V and II-VI semiconductors due to their high Auger, leading to performance degradation. In contrast, IV-VI materials with much lower Auger coefficients can suppress the Auger recombination process at higher temperature, and thus offer better device performance (e.g., higher sensitivity in mid-IR photodetectors), which is significantly important for the modern gas sensing technology development.

It is worth noting that, besides the Auger recombination mechanism, the Shockley-Read-Hall (SRH) recombination, which is also known as defect-assisted non-radiative recombination serves as another important factor in affecting the eventual device per-

formance. It is a two-step process in semiconductors where electrons and holes recombine through defect or impurity energy levels within the band gap. This process has less temperature dependency than Auger. Thus, even intrinsically having the lower Auger process, if the material growth process introduces a high volume of active defects in the material, the devices made out from the IV-VI semiconductor could still end up failing regardless of what temperature it operates. This has remain a major material challenge in IV-VI group material system, especially using high vacuum growth methods that the active voids and dislocations can be created easily. But surprisingly, many studies have found that the IV-VI material produced by the solution-based chemical bath deposition methods could effectively passivate the defects via introducing oxide in the growth process, which was a main reason making uncooled PbSe based MIR photodetectors widely utilized in the past few decades.

1.2 Overview of Chemical Bath Deposition Method

The Chemical Bath Deposition (CBD) method for depositing IV-VI semiconductor (lead sulfide) was pioneered by Emerson Reynolds in 1884 [6]. This method is usually considered as the simple and low-cost film deposition method. In which, the crystal quality due to equilibrium growth is better compared to other methods, regardless of the crystal size [7]. Besides, another obvious CBD advantages is low cost, and can be setup easily since it does not require stringent vacuum systems, plasma generators, and high temperature. The main drawbacks of traditional CBD growth method is its challenges in achieving consistent reproducibility, maintaining precise chemical bath concentrations, achieving thin uniform layers across a large surface, and the process is further restricted by its dependency on the substrate material [8] [9].

It is widely known that, there are mainly two chemical growth mechanisms to grow PbSe using the CBD method, which include Ion-By-Ion (IBI) and Cluster (colloidal)

methods. The Ion-by-Ion (IBI) mechanism involves a reaction between free metal ions (Pb^{2+}) and selenide ions (Se^{2-}) or more likely hydrogen selenide ions (HSe^{-}). This reaction results in the precipitation of PbSe when the ionic product exceeds the solubility product [10]. The reaction process of IBI is expressed as follows [2]:

$$\mathrm{SeSO_3^{2-} + OH^- \rightarrow HSe^- + SO_4^{2-}}$$

$$\mathrm{Pb^{2+} + HSe^- + OH^- \rightarrow PbSe + H_2O}$$

In the cluster mechanism, colloidal particles produced through homogeneous reactions in the solution adhere to the substrate and create a very thin layer. During cluster growth, solid clusters form in the solution, and diffuse to the substrate. At low $[OH]/[\mathrm{Pb^{2+}}]$ ratios, solid oxide clusters form due to $\mathrm{Pb(OH)_2}$ precipitation, which subsequently react with free selenide anions to generate PbSe clusters [11]. At low temperatures, the decreased solubility of Pb-hydroxide leads to the precipitation of $\mathrm{Pb(OH)_2}$, which subsequently reacts with $\mathrm{Se^{2-}}$ to form PbSe nanoparticles. Due to the reduced kinetic energy at low temperatures, the PbSe nanoparticles lack sufficient energy to undergo proper crystallization, causing them to aggregate randomly and form clusters [12].

The chemical reaction process of Cluster is expressed as follows [2] :

$$\mathrm{SeSO_3^{2-} + H_2}O \rightarrow \mathrm{HSe^- + SeS_2}O_6^{2-} + \mathrm{OH^-}$$

$$\mathrm{Pb(OH)_2 + HSe^- \rightarrow PbSe + OH^- + H_2}O$$

Besides two traditional growth mechanism, it is noted that there is a third unique hybrid mechanism which is a combination of both Ion-By-Ion (IBI) and Cluster. We call it as the Oriented Attachment (OA) method. Such an OA process is a crystal growth process in which nanocrystals align and merge, resulting in the formation of a single crystal. Templeman et al. introduced an OA chemical deposition growth

technique to deposit PbSe, which demonstrated substantially improved uniformity and quality [11]. But his OA deposition has to be carried on the GaAs substrates. In recent, our group's graduated member Dr. Tahere Hemati established a new OA growth method which can deposite the OA PbSe film directly on amorphous substrates.

In her work, the growth duration is identified as a crucial parameter that influences the transition between different growth mechanisms, including cluster formation, IBI, and OA. Tahere observed that the cluster mechanism is active during the initial 0 to 3 minutes, after which it transitions to the OA mechanism. The OA mechanism remains dominant for approximately 10 minutes, followed by a subsequent shift to the IBI mechanism. Fig.1.2 illustrates the growth rate as a function of growth time, distinguishing three distinct growth mechanisms: Cluster, OA and IBI[2].

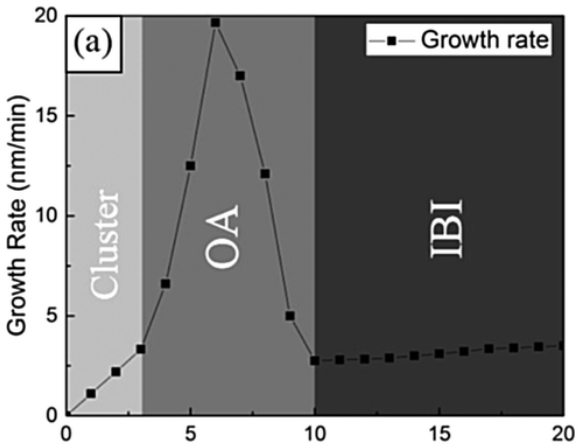

Fig. 1.2: the growth rate as a function of growth times [2]

In the growth experiment of my thesis study, I continued her unique growth work to deposite OA PbSe thin film and further conducted the study on various control factors , including the growth time, growth temperature, and solution pH. Through this study, I developed a systematic understanding of how to regulate the growth mechanism at various stages. A comprehensive discussion of this topic will be presented in the following Chapter Two section.

1.3 Periodic Photonics Engineering

The advancement of nano-fabrication technology has spurred growing interest in chip-scale photonic gas sensors. As shown in Fig.1.3, different gas molecules only absorb a set of very narrow bandwidth light at specific MIR wavelengths, which correspond to their molecular vibration energy levels. However, the gain spectra of the as growth semiconductor films are generally very broad in the wavelength domain.

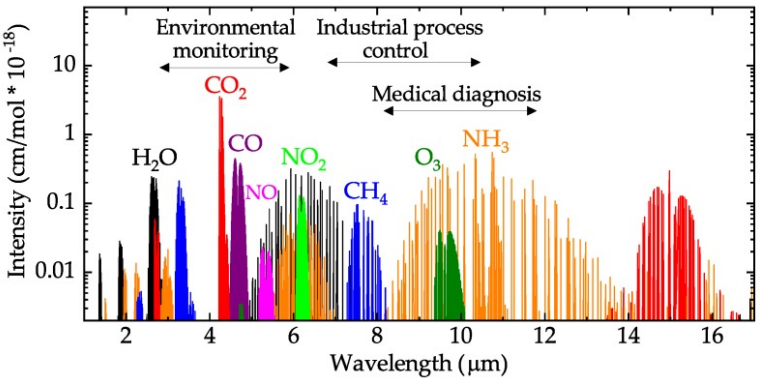

Fig. 1.3: Mid infrared absorption fingerprint of some gas molecules with their relative intensities[3].

Therefore, it is preferable that the optoelectronic devices such as light emitters or photodetectors can be tailored to only respond to a narrow bandwidth in order to achieve a high selectivity in the gas sensing process. Thus, considering the powerful ability to enable the photonic resonance, enhance the Purcell effect and thus manipulate the resonant quality (Q) factor to stimulate light and molecule interaction, periodic photonic engineering, specially the simple 1D resonant grating structure, i.e., high contrast grating (HCG), plays a crucial role in supporting the rapidly developing field of on-chip biological and chemical sensing.

Talking about HCG photonics, it is a periodic sub-wavelength structure composed of a high-refractive-index material embedded in a lower-refractive-index medium, which facilitates strong light confinement, and wavelength selectivity, making it useful for lasers, optical filters, and photonic sensors. Particularly for the photnic gas sensors, I

believe the device performance can be significatnely boosted up with the integration of this photonic engineering solution. Therefore, conducting photonic engineering work using the HCG architecture with the goal to enhance the Q-factor is another important work that I conducted during my master student period, which will be further elaborated in this thesis in the following Chapter four section.

1.4 Research Objectives and Thesis Outline

The objectives of this thesis study focuses on the study of the IV-VI material growth optimization to produce high quality MIR thin films, and the photonic structure design strategy, tailored for gas sensing applications. By integrating a suitable photonic grating structure, this PbSe-based design offers a cost-effective optoelectronic device alternative with improved spectral control.

This thesis explores the growth of PbSe material and nanophotonic engineering of PbSe nanocrystal films to maximize their performance as mid-infrared emitters. This research aims to advance photonic grating engineering using PbSe semiconductors to develop mid-infrared light sources for gas sensing applications.

For the outline of this thesis, the current chapter provides a brief review of the key characteristics of PbSe materials as well the periodic photonic grating to support the device development.

Chapter Two details the experimental process for growing PbSe using the Chemical Bath Deposition (CBD) method using Oriented Attachment technique, with variations in key parameters such as temperature, pH, and growth time. Characterization of the samples was conducted using Scanning Electron Microscopy (SEM), Energy Dispersive X-ray Fluorescence (EDX), X-ray Diffraction (XRD) and FTIR, with photoluminescence (PL) measurements taken to assess the material's properties.

Chapter Three introduce the details of the effect of thermal annealing treatment and investigated how annealing with nitrogen influences the photoluminescence and structural properties of PbSe thin films deposited on a glass substrate.

Chapter Four focuses on the simulation and design of nanostructured photonic gratings, optimizing various parameters to enhance emission. An e-beam resist was coated onto the PbSe sample, followed by mask patterning using Electron Beam Lithography (EBL) to create nanometer-scale features with an optimized beam current and dose. Unwanted PbSe was then removed through dry etching using Reactive Ion Etching (RIE). The characterization of the fabricated sample using SEM, AFM, and FTIR is also discussed. Chapter Five summarizes the overall work and provides recommendations for future research directions.

With the growing need for cost-effective, narrowband emitter, the results of this study could serve as a foundational step toward the development of rapid manufactured infrared sensors and imaging devices.

CHAPTER 2

Material Deposition and Characterization of PbSe Thin Films

In this chapter, I will present my extensive experimental study on preparing the high quality PbSe thin films using chemical bath deposition method. The thin film material serves as the foundation for me to further conduct the design and fabrication of the corresponding emitting devices.

2.1 Experimental Setup for the Chemical Bath Deposition Process

To conduct the chemical reaction process, Pb is used as cation and Se as anion. Sodium hydroxide (NaOH) is used as a complexing agent to control the reaction rate [19]. With that, to prepare the CBD process, several precursor solutions need to be created first with the steps detailed below.

The Pb precursor and the Se precursors are two main solutions for enabling the reaction. For the the Pb precursor, 0.2 M lead (II) acetate trihydrate (Aldrich, Z99.99% trace metals basis) used, which is prepared by adding lead acetate in 250 ml of deionized water and placing on a hot plate at 105 ° C for 15 minutes. After preparation, the Pb precursor bottle is stored in a refrigerator at 4°C. Before use, it should be placed in a warm water bath or on hotplate for a few minutes to allow it to reach room temperature. For the Se precursor, a 0.2 M stock solution of sodium selenosulfate (Na_2SeSO_3) was prepared by adding 0.2 M selenium powder (Aldrich, 100 mesh, 99.99% trace metals basis) with 0.5 M sodium sulfite (Aldrich, BioUltra, anhydrous, $\geq$98% purity). The Na_2SeSO_3 solution was stirred at 105°C for 5 to 6 hours until the solution became transparent in color. Then, it was filtered to remove non-reacted selenium powder. A 5 M NaOH solution was prepared by dissolving sodium hydroxide

in deionized water. The mixture was stirred at 85°C for approximately 30 minutes until the sodium hydroxide was fully dissolved.

Besides, amorphous substrates i.e. rectangular microscopic glass slides 3"x 1" were used as the substrate to facilitation the deposition of the PbSe films. Thorough cleaning of substrates is necessary before the process: The glass slides were cleaned through Acetone (55°C) and Methanol (RT) for 10 minutes and 05 minutes respectively and then by the RCA method. 5 parts of De-ionized water, 1 part of Ammonia Hydroxide and 1 part of Hydrogen peroxide were used.

During the growth experiment, a mixture of DI water and ammonia hydroxide was heated on a hot plate until the solution reached 70°C. Once the target temperature was achieved, hydrogen peroxide was added, and glass slides were immersed in the solution for 15 minutes. The slides were then removed, thoroughly rinsed with deionized water, and dried using ultra-high-purity (UHP) nitrogen gas.

Below listed is a step-by-step process for growing PbSe nanocrystals under the water-bath control environment:

1 Fill a Pyrex crystallizing dish (beaker) with water and place it on a hot plate set to ~ 330°C.

2 . Heat the water bath for 10 to 15 minutes, placing a thermometer inside to monitor the temperature.

3 Once the water bath temperature reaches 85°C, place a solution bottle containing DI water, Pb precursor, and stir bar magnet into the bath. Ensure that two-thirds of the solution bottle is submerged in water. Within approximately 10 minutes, the solution temperature typically rises to 96–98°C.

4 When the solution reaches this temperature range, add NaOH and wait for approximately three to four minutes.

5 . Then, add the Se precursor and immediately remove the bottle from the water bath.

6 Insert a clean glass slide (washed with DI water and dried with N_2 gas) into the solution bottle.

7 Seal the bottle with a cap and place it in a forced air oven at a controlled temperature for a specified duration. Fig.2.2 shows the forced air oven where the temperature is regulated through a built-in temperature controller to ensure uniform heating.

During steps 1-4, for enabling better growth temperature control, I have carried out the growth under two temperature control methods using the hot-plate and the water-bath respectively. Initially, I used the hot-plate method by placing the solution bottle directly on the heated surface. However, I observed that the solution temperature was not uniform within the bottle, which affected the deposition quality. While the hot-plate method allowed for faster heating, it resulted in non-uniform deposition due to uneven temperature distribution.

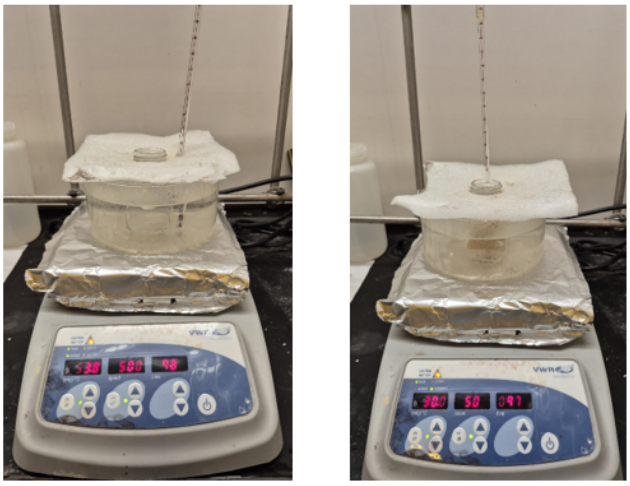

Fig. 2.1: Water bath setup images showing (a) the condition before adding OH and (b) the state after OH addition.

To improve uniformity, I later switched to the water-bath method, where the solution bottle was immersed in heated water as display in Fig.2.1. This approach provided slower, more controlled heating, ensuring a stable temperature throughout the solution. The results showed significantly better deposition uniformity, making the water-bath method ideal for precise temperature control, particularly for nanocrystal growth.

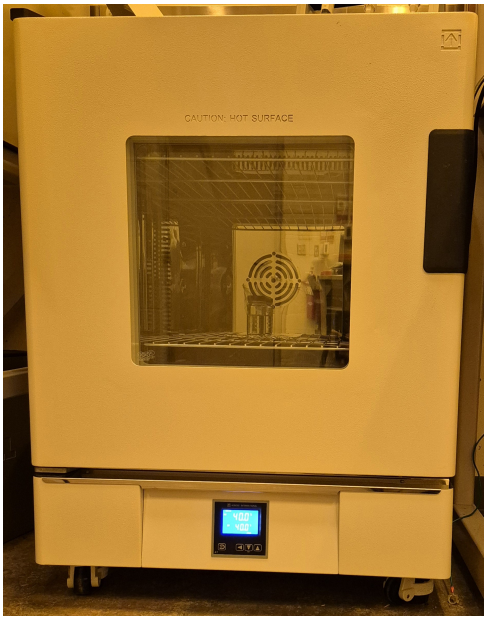

Fig. 2.2: Forced air oven used for growing PbSe

After deposition, the backside of the substrate is scraped away using a blade or cleaned using cotton swabs moistened in nitric acid to ensure accurate analysis of the front layer and to inspect the film's darkness under the light. Afterward, the glass substrates are washed with deionized water to remove any remaining contaminants, and dried with a flow of nitrogen gas, then stored in sample boxes for future use and further characterization.

Following this standardized growth procedure, I varied several growth parameters to study the control of PbSe nanocrystals. The parameters include temperature, pH (NaOH concentration), and growth duration. The detail resulting effects via tuning these parameters will be presented and discussed in the following sections. In certain samples, the same process was repeated to achieve thicker film formation.

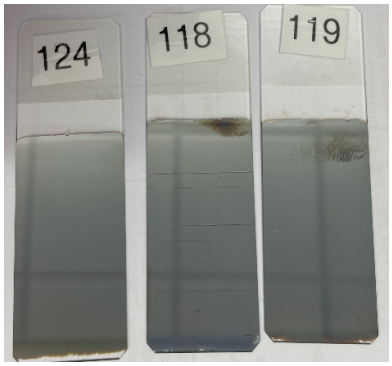

Fig. 2.3: Images of PbSe thin film samples deposited on glass, showing temperature variation from left to right: 65°C, 60°C, and 55°C.

2.2 Investigate the oven temperature effect on the resulting films

The PbSe growth temperature in the forced air oven was varied from 55°C to 65°C. The Fig.2.3 and Fig.2.4 illustrate the impact of temperature on the deposition of PbSe thin films on a glass substrate. The surface of the low-temperature growth Sample #119 (55°C) appears rougher. As shown in Figure 2.4, low growth temperatures (55°C) lead to the formation of clusters due to reduced solubility, which hinders proper crystallization and results in nanoparticle aggregation. As the temperature increases, the crystal size grows, with more pyramid-shaped crystals observed at higher temperature (Sample #124). An increase in temperature results in a corresponding growth in size [13]. The growth temperature typically influences the reaction rate and the structural characteristics of the films [12, 14].

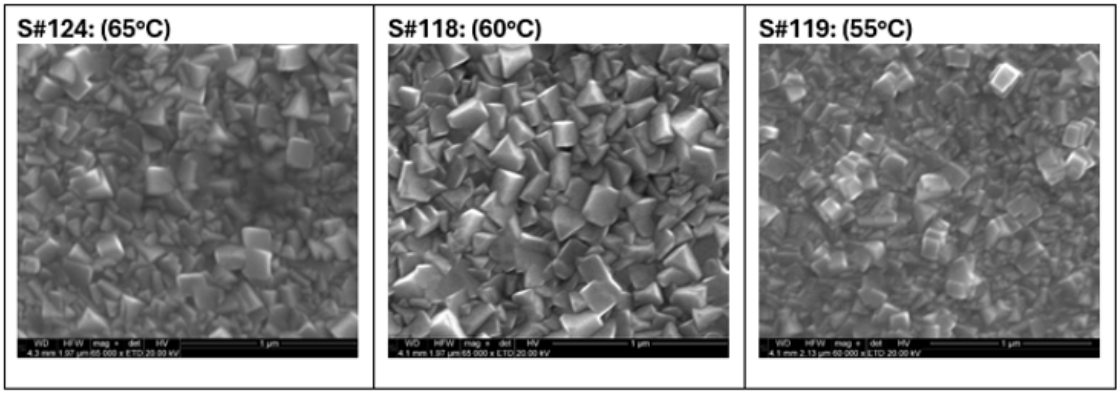

Fig. 2.4: SEM images showing temperature variation in samples

2.3 Investigate the DI water ratio on the resulting films

PbSe was grown by varying the water concentration, with precise control using a pipette. A higher increase in water content appears to promote larger cubic crystal size, greater spacing between crystals, and a transition to an ion-by-ion growth mechanism. Among the samples, Sample #118 (with 21.2 mL of water) exhibits the highest shininess and a greater number of pyramid structures. A lower concentration due to excess water promotes Ostwald ripening, where smaller nanoparticles dissolve and larger ones grow, as shown in Sample #114 in Fig.2.5.

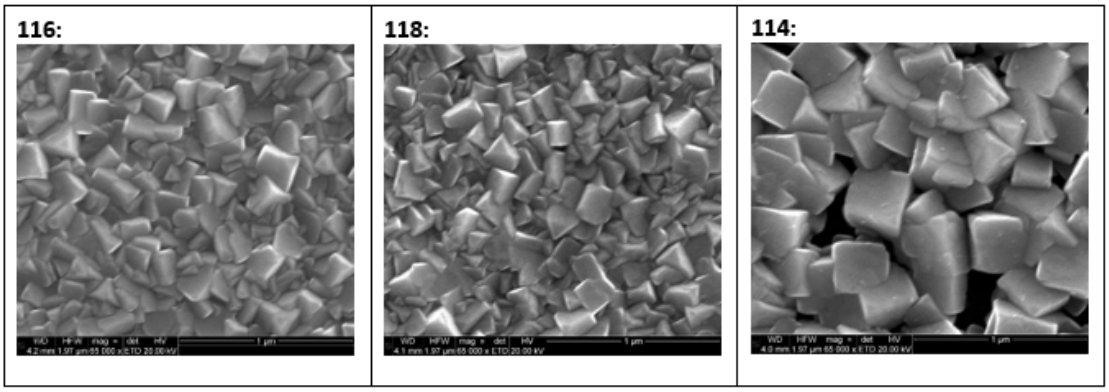

Fig. 2.5: SEM Images of PbSe thin film samples deposited on glass, showing DI water variation from left to right: 20.8, 21.2, and 21.5 ml.

The Fig.2.6 illustrates the photoluminescence (PL) behavior of PbSe samples deposited with varying quantities of deionized (DI) water, while keeping all other growth parameters constant. Sample #118, which was prepared with an optimal amount of DI water, shows enhanced PL intensity due to the formation of OA nanocrystals with improved crystallinity and reduced defect density. In contrast, Sample #116, prepared with less DI water, leads to faster deposition of PbSe, which might trap more defects and thereby reduce the PL. On the other hand, Sample S#114, which was prepared with a higher amount of DI water, shows lower PL intensity. The excessive dilution reduces the precursor concentration, leading to fewer nucleation sites and the growth of larger, less quantum-confined crystals during recrystallization. These larger crystals

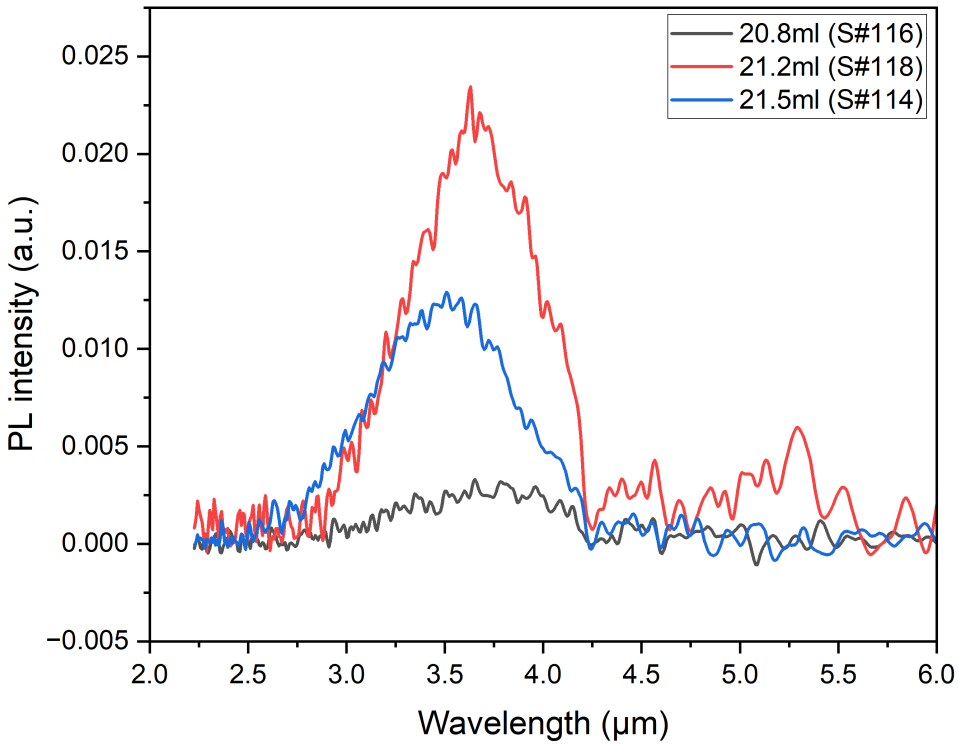

Fig. 2.6: Measurement of PL with variation of DI water during growth process

tend to have lower PL due to reduced carrier confinement and increased non-radiative recombination.As shown in the Fig.2.5 and 2.6, an optimal increase in DI water content results in the formation of smaller nanocrystals, enhancing quantum confinement effects and leading to improved PL intensity.

2.4 Investigate the effect of OH concentration on the resulting films

PbSe thin films were grown by varying the OH^- concentration while keeping all other parameters constant. Table 2.1 presents the recipe for each sample prepared with different OH^- quantities. To assess thin film thickness, samples were examined under light by evaluating their darkness and transparency. The transparency of Samples #128 and #129 is similar to that of Samples #126 and #127, whereas Sample #118 exhibits a noticeably darker transparency compared to the others.

Table 2.1: Change in OH quantity by keeping temperature and water quantity same

Sample No.	Temperature(°C)	DI water (ml)	OH (ml)
129	60	21.2	1.65
118	60	21.2	1.75
128	60	21.2	1.85
126	60	21.2	1.95
127	60	21.2	2.05
130	60	21.2	2.25

The analysis suggests that the optimal window for high-speed growth may be around an OH^- concentration of 1.75 mL. As shown in Figures 2.8 and 2.9, increasing the OH^- concentration results in higher transparency, which is undesirable for our application. Additionally, SEM analysis in fig. 2.10 of Sample #130 (2.25 mL OH^-) reveals irregular crystal sizes, indicating that excessive OH^- leads to non-uniform growth.

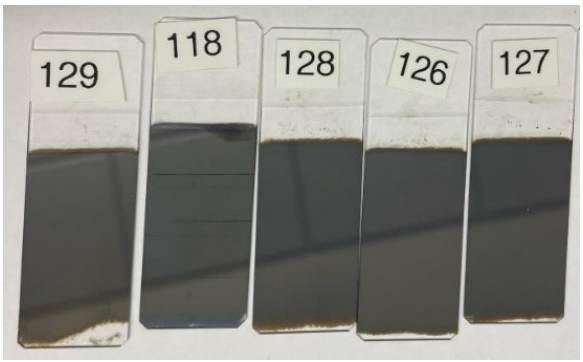

Fig. 2.7: PbSe thin film samples deposited on glass, showing variation in OH quantity.

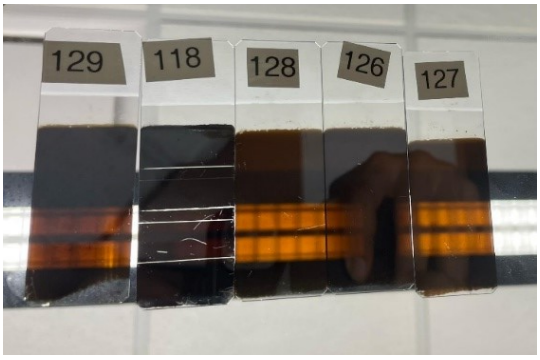

Fig. 2.8: PbSe thin film samples synthesized with varying OH concentrations, displayed under light.

The Fig.2.11 shows the photoluminescence (PL) intensity of PbSe samples deposited with varying OH^- concentrations, while keeping other parameters constant. All sam-

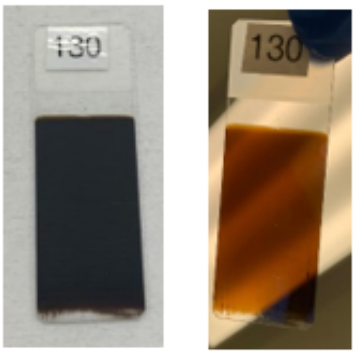

Fig. 2.9: Images of PbSe thin film sample deposited on glass, deposited with higher OH.

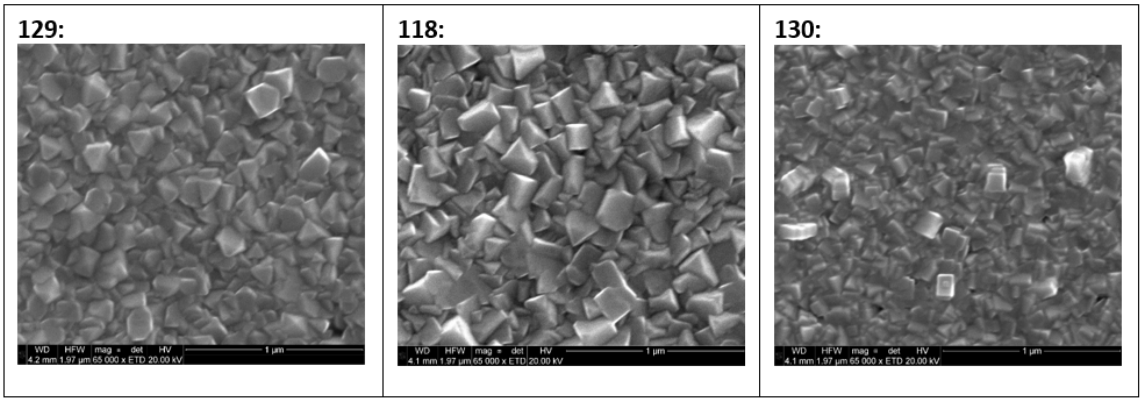

Fig. 2.10: SEM images of PbSe thin film samples deposited on glass, showing the effect of increasing OH quantity from left to right.

ples were prepared at a high temperature of 60 °C. At high OH^- concentration, an abundance of free hydroxide ions can slow down the formation of lead hydroxide nanocrystals, favoring an *ion-by-ion* growth mechanism. This slower growth results in lower PL intensity due to fewer nucleation sites and potentially less uniform crystallite formation. In the case where **1.75 mL** of OH^- was added, the growth mechanism transitions from a cluster-based mechanism to an OA mechanism, which completes effectively within the 10-minute growth window. This condition promotes better crystallinity and particle uniformity, resulting in stronger PL intensity. In the third scenario, with a reduced amount of OH^-, there are fewer hydroxide ions available to combine with lead, leading to an excess of free Pb^{2+} ions. This imbalance causes premature and uneven formation of lead hydroxide prior to the addition of selenosul-

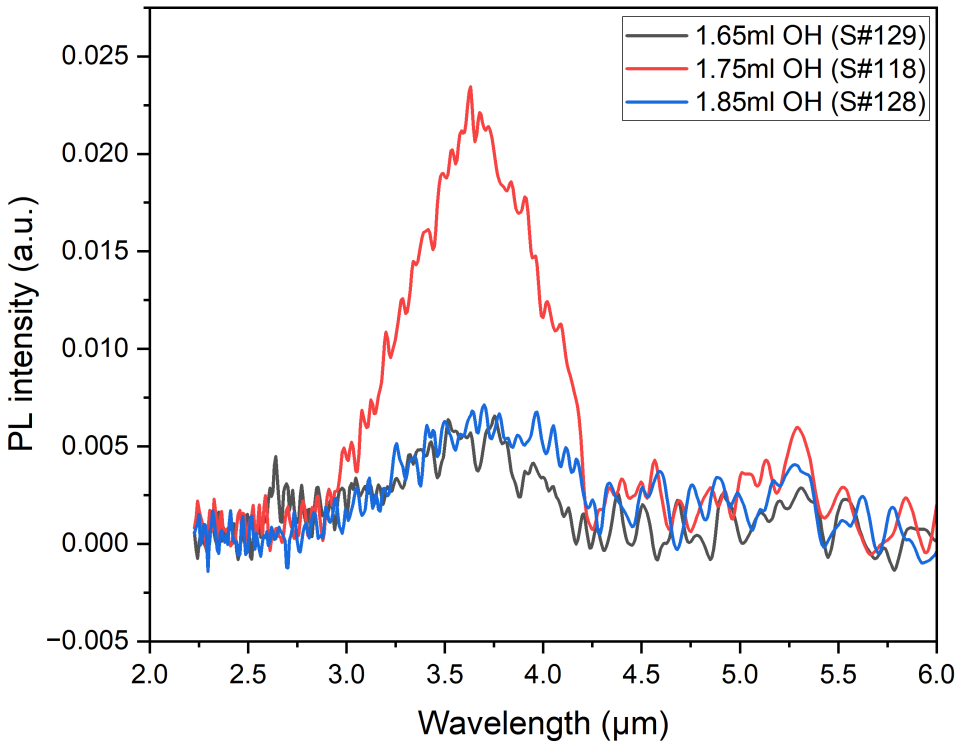

Fig. 2.11: Measurement of PL with variation of OH quantity during growth process

fate, resulting in irregular PbSe crystal sizes, thinner film deposition, and weaker PL emission.

2.5 Investigate the repeated growth process on the resulting films

This section provides a comparative analysis of single and double layer PbSe thin films grown using the chemical bath deposition (CBD) method. This study evaluates their structural, optical, and electrical properties to determine the impact of layering on film performance.

The choice between PbSe single and double-layer films affects the efficiency of the material, making a comparative study essential. PbSe thin films were synthesized using the CBD method under controlled conditions. Two sets of samples were prepared.

One with a single-layer deposition and the other with a double-layer deposition. The deposition parameters such as bath composition, oven temperature, growth recipe and time were maintained constant.

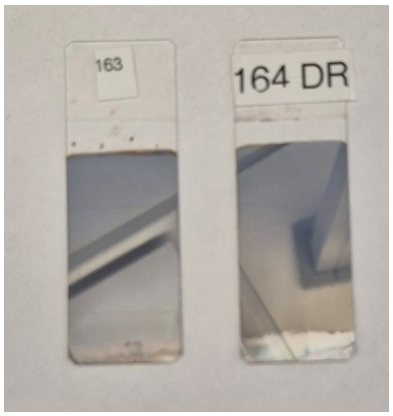

Fig. 2.12: Single Layer (left) and Double Layer (right) PbSe thin Film deposition using CBD method

The Fig.2.12 and Fig.2.13 display single-layer and double-layer PbSe samples. Two single-layer PbSe samples were prepared, after that one of which was used as a substrate in a new solution for double layer deposition. A new deposition solution must be prepared using the same recipe as before, as lead and selenide were consumed and deposited onto the previous sample.

Fig. 2.13: Single Layer (left) and Double Layer (right) PbSe thin Film deposition under the light

Fig.2.12 illustrates the uniform adhesion of the PbSe thin film on an amorphous surface. In Fig.2.13, the single-layer deposition appears as a transparent orange, indicat-

ing that the film is thin. In contrast, a double-layer deposition results in a significantly thicker film, as evidenced by its completely dark appearance under light.

Thickness of both single and double layer samples were measured by the Alpha-step profilometer. The single and double layer thickness was found to be 175 nm and 494 nm, respectively.

The Photoluminescence (PL) measurement was performed using a Bruker Invenio-R Fourier Transform Infrared (FTIR) spectrometer with a resolution of 16 cm^{-1}. The InSb high-gain detector was cooled with liquid nitrogen, while an external SR-830 lock-in amplifier was integrated with the PL module to minimize thermal background noise. Excitation was performed using a 980 nm semiconductor diode laser.

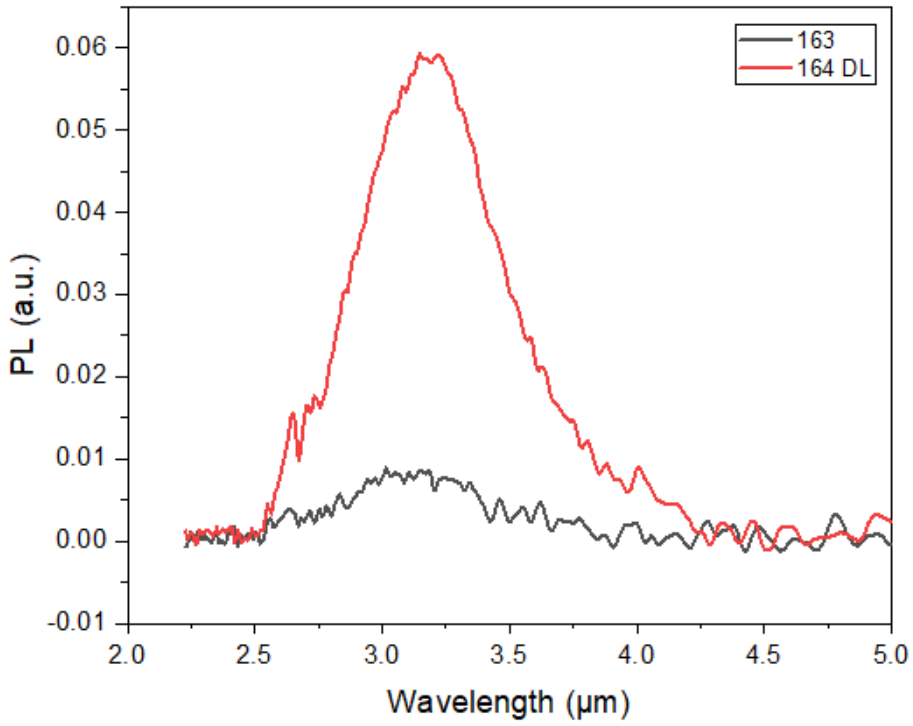

Fig. 2.14: PL measurement of Single Layer and Double Layer PbSe thin Film deposition

An enhancement in PL intensity was observed after the deposition of second layer. Fig.2.14 illustrates the comparison of PL between single-layer and double-layer PbSe thin films. The PL significantly improved after depositing the double layer due to

reduced defects and enhanced radiative recombination.

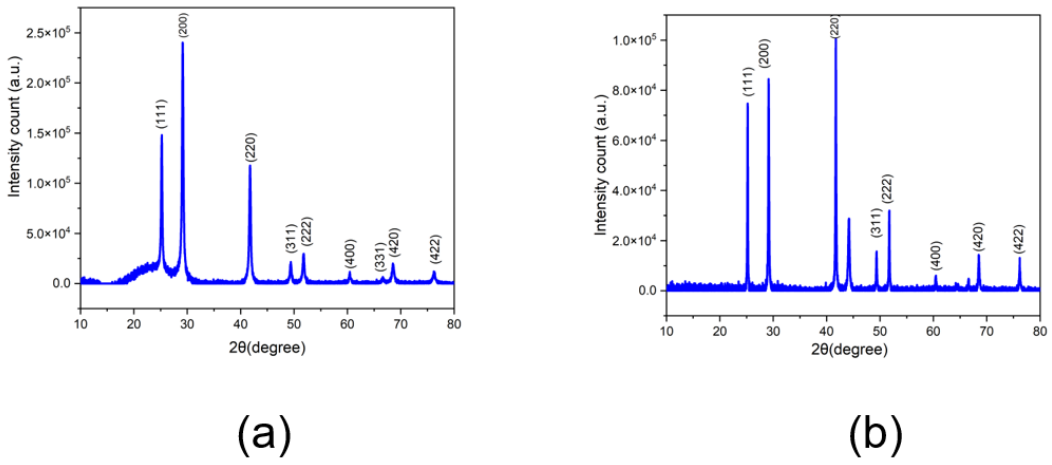

Fig. 2.15: Comparison of XRD of PbSe nanocrystals of (a)single and (b)double layer deposited on Glass substrate

The structural properties of the sample were analyzed X-ray diffraction (XRD). XRD analysis revealed differences in crystallinity between the single and double layer films. The single layer film exhibited a cubic PbSe phase with a preferential orientation along the (200) plane. The double layer has a peak at (220) plane. The double layer film showed increased grain size due to the additional layer. The average crystal size found using the Debye Scherrer equation 2.1 for the single and double layer films are 25.3 and 48.5 nm respectively.

2.6 Investigate the PbSe Films with a Sputtered Seed Layer

This section explores the impact of the seed layer on the optical and structural characteristics of PbSe deposited using the CBD method. The thin film deposited using the CBD method is typically around 200 nm. However, our simulation design for creating photonic structure of PbSe requires a PbSe film thickness of approximately 770 nm. To achieve this, there are two possible approaches: either repeat the deposition process four times or first grow a seed layer and then use the CBD method. Since

each round of CBD increases surface roughness, I opted for the latter approach, i.e. growing an initial seed layer via sputter deposition before depositing PbSe using the CBD method. Similar method has been carried out by Parisa et al. to grow another semiconductor material, zinc oxide which has applications in photodetectors and gas sensors [15].

The sputter deposition is a physical vapor deposition (PVD) method for thin film. In our cleanroom lab, the system we used to deposit PbSeis a built-in-house multi-mode coating system with the sputtering function as shown in Fig.2.16.

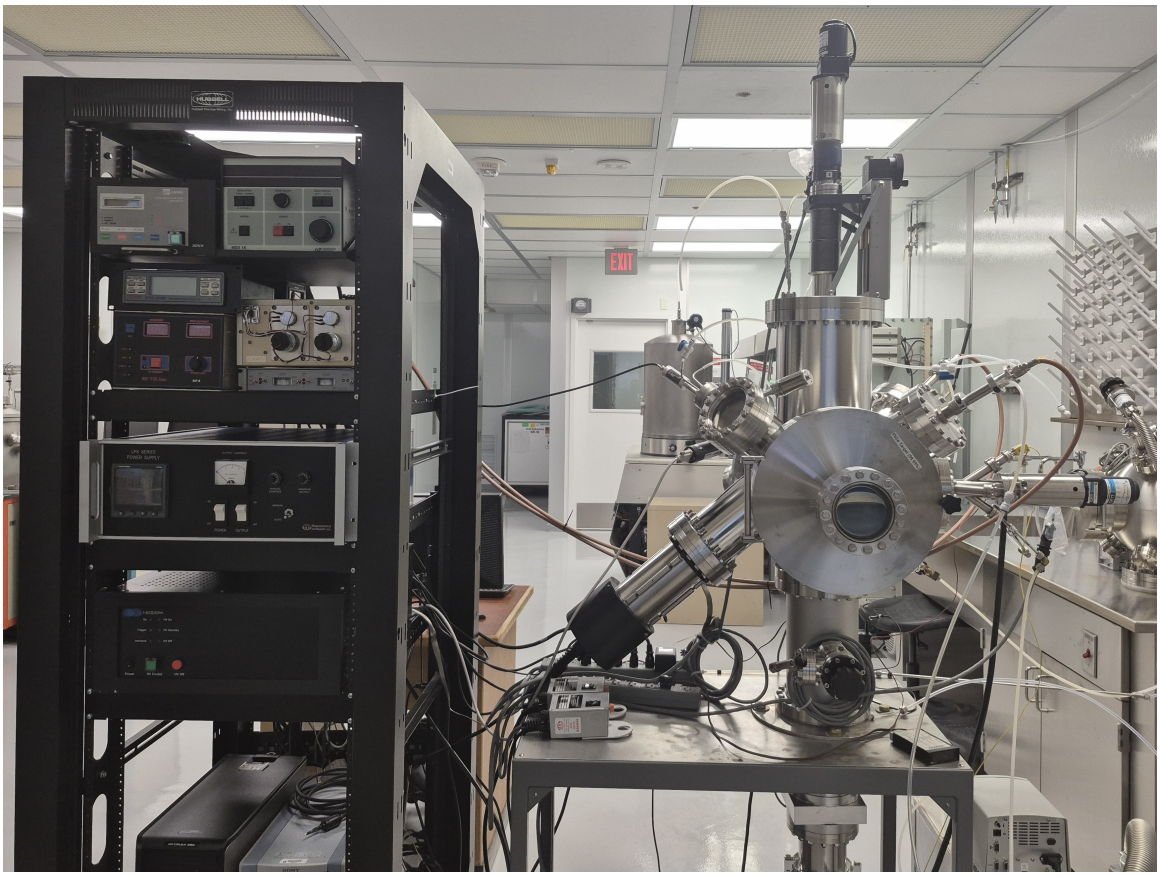

Fig. 2.16: The multi-mode pulsed E-beam/Sputtering Deposition System

To carry out the seed-layer deposition experiment, we prepared both glass and silicon samples as the substrates, which were cut into 1×1 cm^2 pieces using a dicing machine and thoroughly cleaned prior to deposition. The cleaning process involved solvent cleaning followed by plasma treatment to ensure the removal of any residual

contaminants. For solvent cleaning, samples were placed in an ultrasonic cleaner and sequentially cleaned with acetone, methanol and isopropyl alcohol (IPA), each for five minutes. Following this, they were rinsed in deionized water for three minutes and dried using ultra-high-purity (UHP) nitrogen gas.

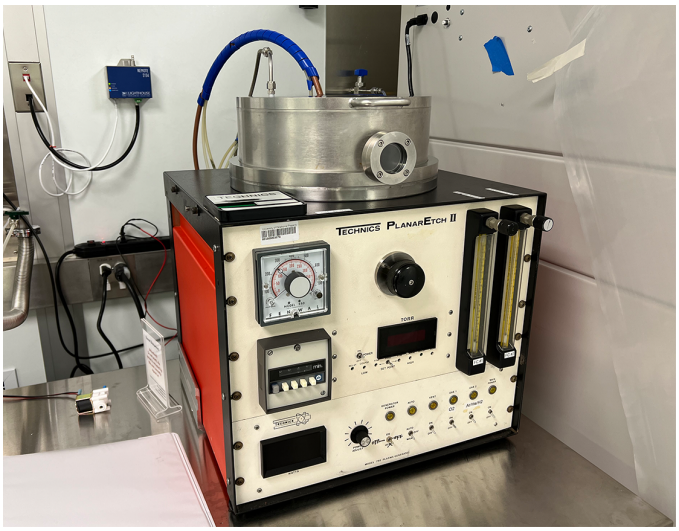

Fig. 2.17: Technics Plasma Asher

To further enhance cleanliness, a Technics Plasma Asher (fig.2.17) was used with a setting of 100W at 200 mTorr for three minutes. This process effectively removed any remaining contaminants. Oxygen gas was introduced, causing any residual inorganic matter to be converted into ash, primarily composed of carbon oxides and water vapor, which were subsequently evacuated by the vacuum pump.

The cleaned samples were then loaded into the deposition chamber, where PbSe thin films were deposited using an RF magnetron sputtering system. The deposition was carried out on glass and Si substrates (10 mm $\times$ 10 mm) using a PbSe target (99.9% pure). The vacuum pressure in the process chamber was maintained at 1×10^{-3} Torr, while the working pressure was set at 2×10^{-2} Torr. The target-to-substrate distance was kept at 20 mm to ensure optimal film growth conditions.

Through measuring under the profilometer, thickness of 300 nm measured of PbSe

layer,deposited on silicon and glass substrates by sputtering. This was followed by two rounds of deposition via the chemical bath method to achieve the desired thickness. The results and comparisons are presented in the next section. The parameters set in RF magnetron sputtering system for PbSe deposition are shown in Table 2.2.

Table 2.2: Parameters for RF magnetron sputtering of PbSe thin films on Glass and Si substrates.

Power	25 Watt
Deposition rate	2.8 A/s
Deposition time	33 mins
Growth temperature	300 °C
Target-substrate distance	20 mm
Argon flow rate	0.03 SLPM
Working pressure	2×10^{-2} Torr
Vacuum pressure	1×10^{-3} Torr

The thickness was measured using a profilometer. To facilitate the measurement, I created a mark on the sample with a blade, allowing the stylus needle to precisely scan across the marked area and determine the thickness. The profilometer, also known as a thickness profiler, is used as a measuring device to determine depth. The Profiler Model: D-500 was used. It consists of a stylus that can be positioned on the sample and moved perpendicular to the interface plane where depth measurements are required. As the profilometer traces over the sample, it detects variations in depth, allowing for accurate depth determination. This specific type of profilometer is referred to as a contact profilometer. The profilometer scan parameters were: speed of 0.03 mm/sec, length of 0.5 mm, stylus force of 0.20 mg, and forward direction.

Using the CBD method, the double-layer PbSe deposition resulted in a final thickness of 750 nm, indicating a growth rate of approximately 21 nm/min. The figure 2.19 displays final thickness which is around 750nm measured by KLA Tencor Profiler Model: D-500.

Fig.2.20 presents a comparison of PbSe thin film deposition on glass and silicon substrates, featuring a double-layer CBD on a seed layer. It should be noted that sputter-

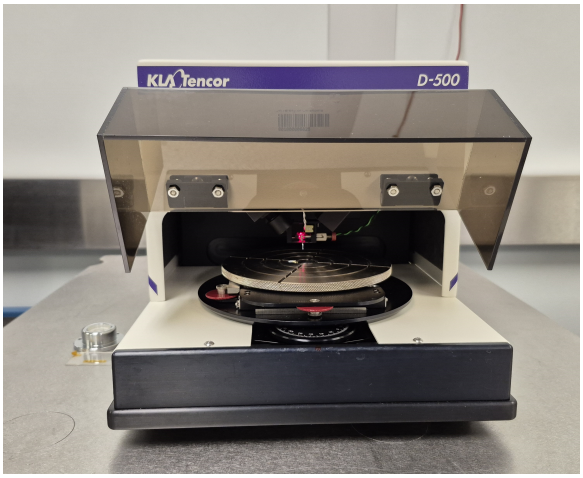

Fig. 2.18: KLA Tencor Profiler Model: D-500

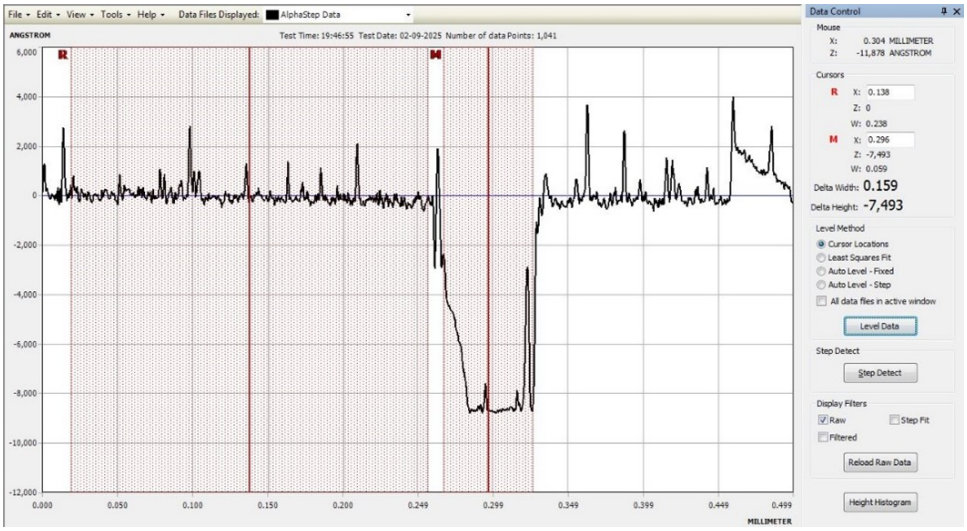

Fig. 2.19: Thickness measurement after double layer CBD on Sputtered seed layer

deposited samples exhibit no PL intensity without the OA-deposited layer.

The PL intensity of the deposited PbSe is significantly enhanced in the silicon sample. The emission spectrum in the silicon sample appears broader compared to the glass sample, where the PbSe film exhibits a narrower and smoother spectrum. Another notable observation is the shift in peak position. PbSe deposited on glass shows a peak at 3.1 µm, whereas in the silicon sample, the peak is shifted to approximately 3.6 µm. This shift suggests a potential influence of substrate properties on the optical characteristics of the PbSe thin film.

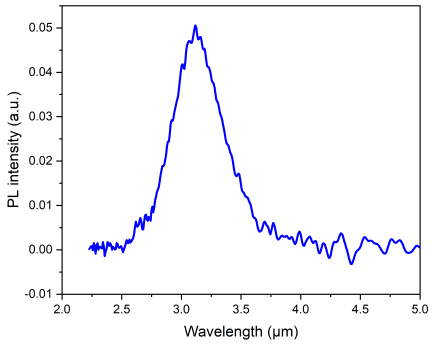

(a) PbSe thin film deposited on Glass substrate

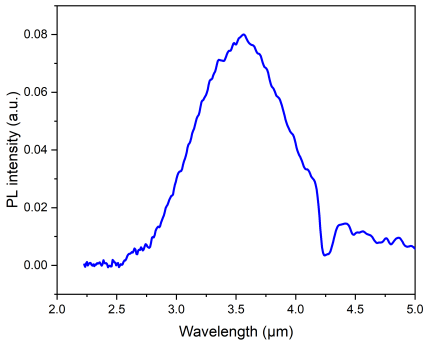

(b) PbSe thin film deposited on Silicon substrate

Fig. 2.20: Comparison of photoluminescence (PL) of PbSe deposited by chemical bath deposition (CBD) on a sputtered seed layer with glass and silicon substrates.

PbSe thin films were deposited on glass and silicon (Si) substrates with a sputtered seed layer as the initial deposition. The SEM and XRD images are shown in fig.2.21 of the sputtered samples, which show their surface morphology.

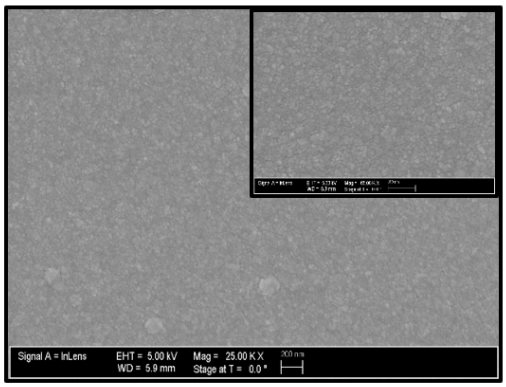

(a) SEM of PbSe thin film deposited on Glass substrate

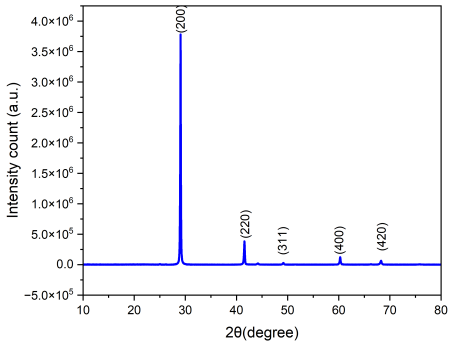

(b) XRD of PbSe thin film deposited on Glass substrate

Fig. 2.21: SEM and XRD image of PbSe thin film deposited by Sputtering at 300°C.

The XRD patterns showing (200) peak of PbSe nanocrystals deposited at 300 °C by sputtering. The average crystal size, D, was determined using the Debye–Scherrer equation [16]:

$$D = \frac{0.9\lambda}{B\cos\theta} \tag{2.1}$$

where λ is the wavelength of the X-ray radiation ($\lambda = 1.5406$ Å), B represents the full

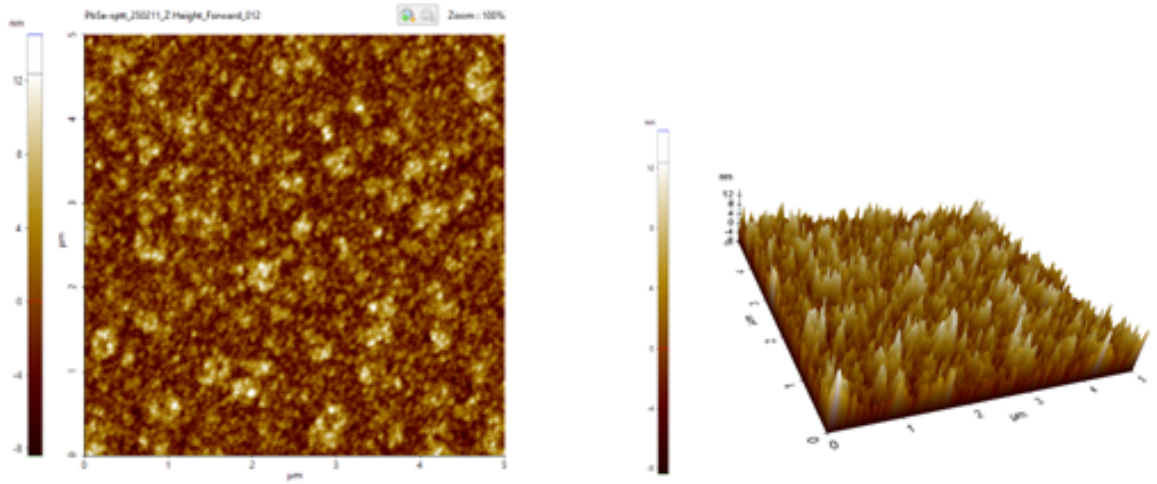

(a) AFM 2D image of PbSe thin film deposited by sputtering

(b) AFM 3D image of PbSe thin film deposited by sputtering

Fig. 2.22: 2D and 3D AFM images of PbSe deposited by sputtering on glass substrate.

width at half maximum (FWHM), and θ is the diffraction peak angle.

The average crystal size found for PbSe sputtered sample 39.6 nm respectively. The lattice constant, a, for the cubic structure was calculated using:

$$a = d\sqrt{h^2 + k^2 + l^2} \tag{2.2}$$

where d is the interplanar spacing, and (hkl) are the Miller indices.

Figures 2.23, 2.24, 2.25 are the SEM and AFM 2D and 3D images of PbSe nanocrystals deposited by CBD method on Sputter seed layer on glass and Silicon substrates. PbSe thin films with same thicknesses (around 750nm) were deposited on silicon and glass substrates. The SEM images at magnification 25000x and 65000x are shown below.

The surface roughness of the sputtered sample and the PbSe nanocrystals deposited via the CBD method on the sputtered sample is presented in table 2.3.

where Rpv is (peak-to-valley of the line) difference between min and max, Rq is root-mean-squared roughness and Ra is average roughness.

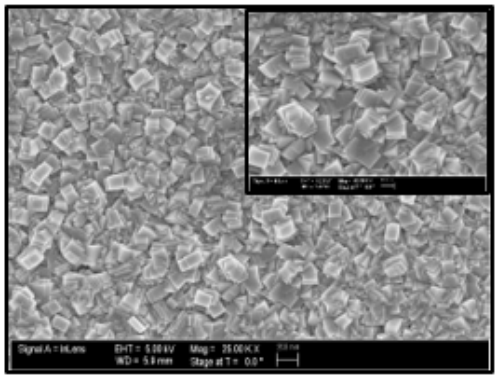

(a) PbSe thin film deposited on Glass substrate

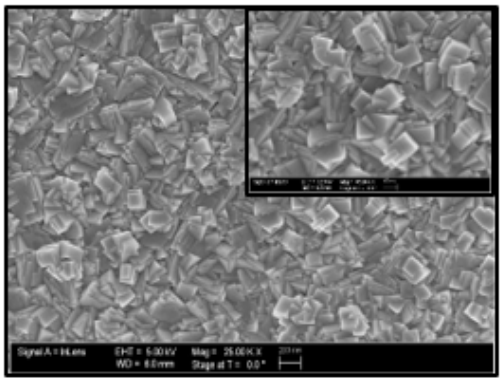

(b) PbSe thin film deposited on Silicon substrate

Fig. 2.23: Comparison of SEM images of PbSe deposited by chemical bath deposition (CBD) on a sputtered seed layer with glass and silicon substrates.

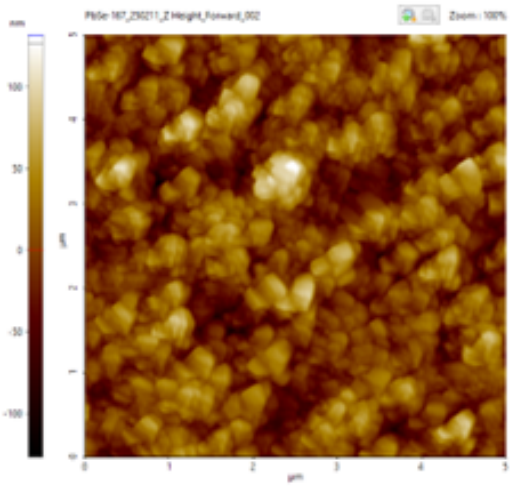

(a) PbSe thin film deposited on Glass substrate

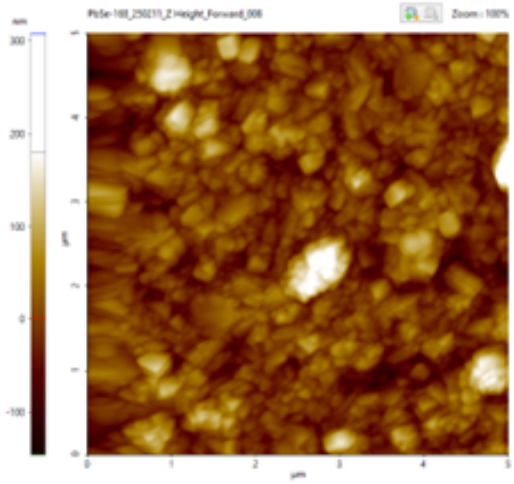

(b) PbSe thin film deposited on Silicon substrate

Fig. 2.24: Comparison of AFM 2D images of PbSe deposited by chemical bath deposition (CBD) on a sputtered seed layer with glass and silicon substrates.

Table 2.3: Surface roughness of PbSe samples.

Sample	Min(nm)	Max(nm)	Mid(nm)	Rpv	Rq	Ra
Sputtered sample	-8.4	14.5	3.0	22.8	3.1	2.5
CBD on Sputt. (Glass)	-126.5	131.6	2.5	258.1	32.3	25.9
CBD on Sputt. (Silicon)	-146.3	308.3	80.9	454.6	46.0	33.8

The XRD results in fig.2.26 indicate that the peak intensity of PbSe is higher on the glass sample compared to the silicon sample. This may be attributed to the lower X-ray absorption of glass compared to silicon, allowing greater X-ray penetration and

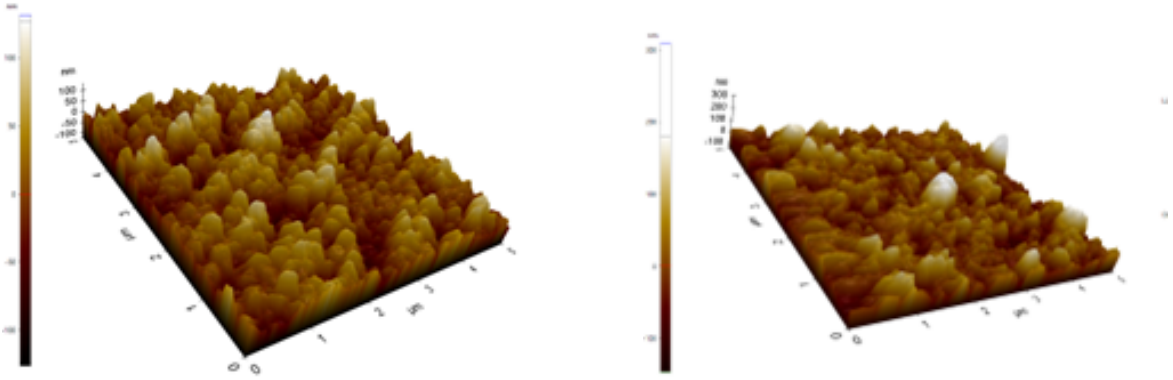

(a) PbSe thin film deposited on Glass substrate

(b) PbSe thin film deposited on Silicon substrate

Fig. 2.25: Comparison of AFM 3D images of PbSe deposited by chemical bath deposition (CBD) on a sputtered seed layer on glass and silicon substrates.

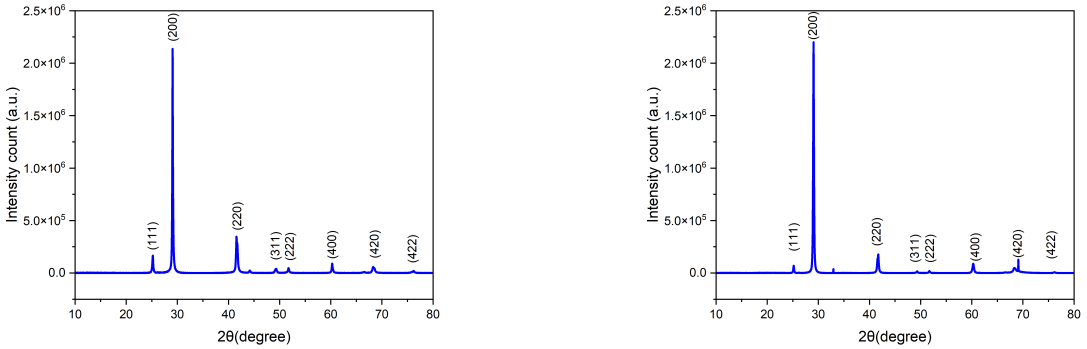

(a) XRD of PbSe thin film deposited on Glass substrate

(b) XRD of PbSe thin film deposited on Silicon substrate

Fig. 2.26: Comparison of XRD of PbSe deposited by chemical bath deposition (CBD) on a sputtered seed layer on glass and silicon substrates.

resulting in stronger PbSe diffraction signals. The average crystal size found using the equation 2.1 for CBD on Sputter(glass) and CBD on Sputter(silicon) samples are 27.7 and 28.2 nm respectively.

CHAPTER 3

Post Annealing Study on the CBD Prepared PbSe Films

Annealing is a common but effective technique to improve the properties of thin films including PbSe [17, 18, 19, 20, 21], leading to changes in structural, electrical, morphological, and optical properties[22]. For example, F Zhao et.al performed heat treatment with oxygen on Molecular Beam Epitaxy (MBE) grown monocrystalline PbSe films and mentioned that due to formation of oxidation layer, PL intensity significant increased after oxygen annealing at higher temperature [17]. Jarod et al. conducted thermal annealing under a nitrogen of PbSe thin films deposited on GaAs using Molecular Beam Epitaxy (MBE) at low temperature. They found that annealing at 325°C resulted in the highest photoluminescence intensity and notable changes in grain boundaries [20]. In addition, C.K. Bandoh et al. deposited lead selenide films on glass substrate using the Chemical Bath Deposition method and subjected them to heat treatment in air at 300°C. Their findings indicate that annealing enhances structural and optical properties, leading to an increase in crystal size and a reduction in band gap [21].

Following the material growth study, in this section of my thesis, I investigated how annealing influences the structural properties and photoluminescence of PbSe nanocrystals films prepared via our modified Chemical Bath Deposition method.

3.1 Annealing Experiment

In this work, I started with the sample #131. The as-grown wafer was cut into four small pieces, and subjected to heat treatment on a hot plate at four different temperatures (200°C, 250°C, 300°C ,and 350°C) for 5 minutes. The as-grown PbSe samples prepared by our modified CBD method were shinny, mirror-like, and gray in

color. After the annealing process, the color of films changed from grey to dark-brown as shown in Fig.3.1.

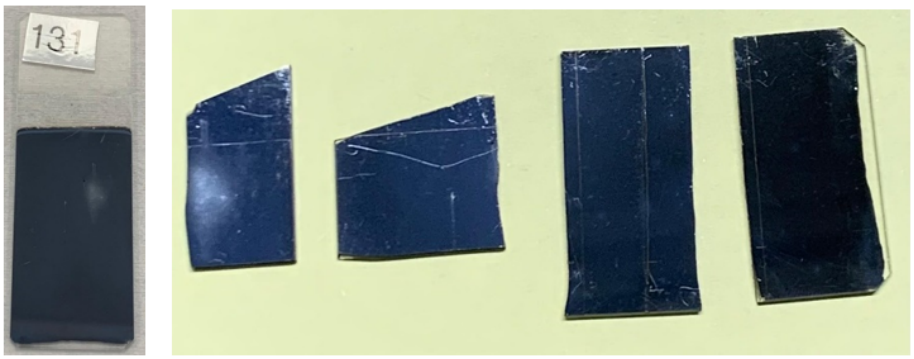

Fig. 3.1: Comparison of sample after heat-treatment in air

The PL at these four different temperature is shown in Fig.3.2. No PL was detected of the as-grown PbSe and after heat treatment, PL improves. Fig.3.2 shows that PL rises gradually from 200°C and reach maximum at 300°C and significantly decrease at 350°C.

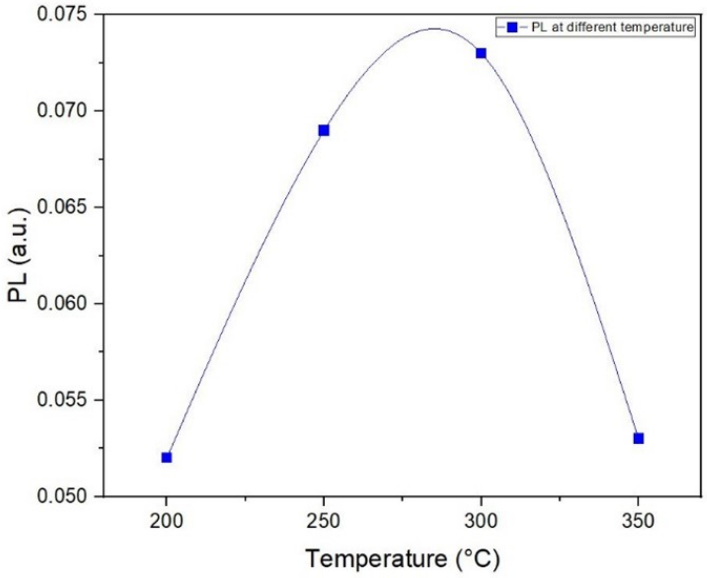

Fig. 3.2: PL Signal vs hot-plate temperature for 05 mins

The PbSe sample, when heated in air, undergo oxidation, leading to the formation of lead oxide (PbO) and selenium dioxide (SeO_2). These oxidation products likely

alter the surface chemistry of the sample, resulting in a darker appearance. Another contributing factor could be the loss of selenium, which is volatile at elevated temperatures, especially in an oxidative environment, where it forms SeO_2. The loss of selenium affects the stoichiometry of the PbSe nanocrystal film, potentially creating lead-rich or oxidized regions that appear darker. To prevent the darkening and further improve the PL of the PbSe samples, annealing was then carried out in a tube furnace under the pure nitrogen environment Fig.3.3.

The Fig.3.3 shows the tube Furnace which is connected on one end with the Nitrogen gas cylinder. The mass flow controller is connected between the Nitrogen gas cylinder and the furnace to control the gas flow rate with provision of small valves to control the gas. The other end of furnace is connected to vacuum and the glass bottle filled with water.

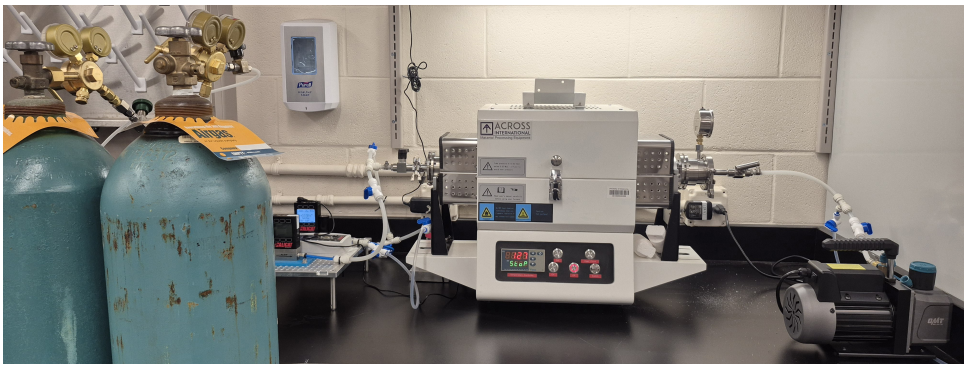

Fig. 3.3: Thermal annealing treatment setup

In this study, we selected as-grown PbSe sample #138. Generally, the thin films were annealed under Nitrogen gas for duration of 30 minutes at different temperatures varying from 275 °C to 350 °C. Firstly, I put the glass slide with the PbSe sample on the top, on the boat-shaped crucible inside the tube. Secondly, Alumina ceramic thermal blocks should be placed on both ends of the furnace tube. This will form a balanced temperature field in the furnace and also prevents the tube O-rings to deteriorate at higher temperatures. Thirdly, vacuum is created in the tube through vacuum pump in the furnace to get rid of any particles or gas like oxygen, carbon dioxide etc. This

will prevent oxidization and contamination on the sample surface and maintain quality surface. The purpose of placing glass bottle with water on other end of tube furnace is to ensure that gas is flowing through the furnace by seeing gas bubbles in water. An examplified time-temperature graph for annealing temperature is shown in Fig.3.4.

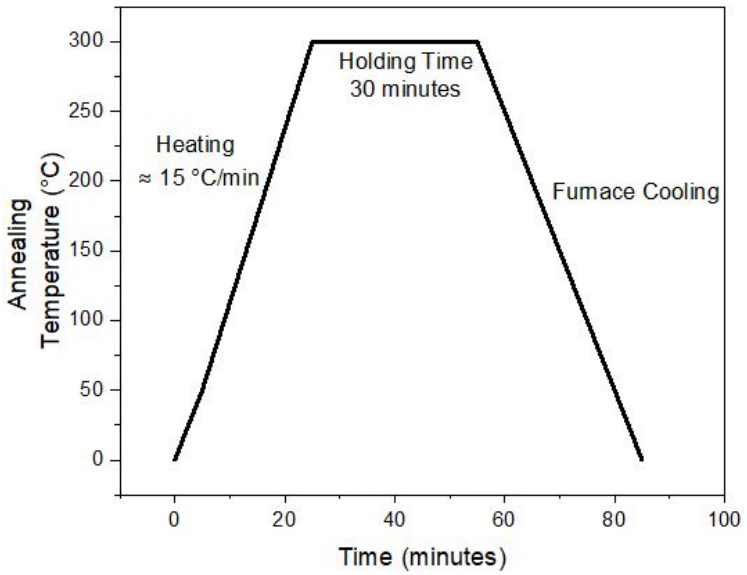

Fig. 3.4: Annealing time-temperature graph for PbSe thin film

3.2 PL, SEM and XRD characterization

In sample #138 which is a repeated grown layer PbSe, the measured PL intensity of as-grown sample was 0.03 a.u. The samples were cut in the size of 5×5 mm^2 using the dicing machine and placed into the furnace, heated to the desired temperature, and then allowed to cool down to room temperature. The samples were taken out for further characterization. The heat-treatment under nitrogen gas was performed with flow rate of 0.1 LPM at different set temperatures (275°C, 300°C, 325°C and 350°C).

The PbSe sample was annealed under nitrogen gas at various temperatures. Prior to annealing, the photoluminescence (PL) intensity was relatively weak compared to the annealed samples. As shown in Fig. 3.5, a strong PL peak was consistently observed at around 3.7 µm for all annealing temperatures.

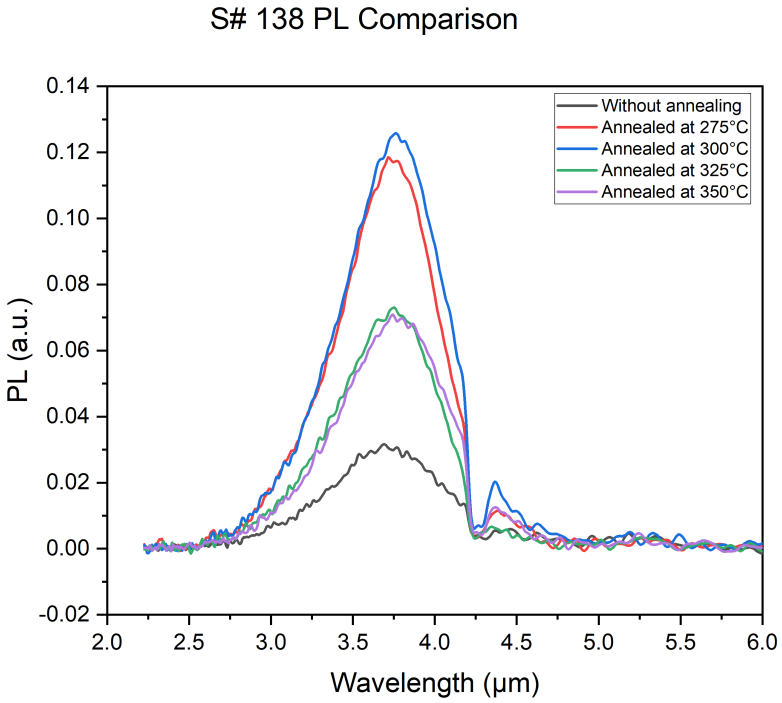

Fig. 3.5: PL measured of As-grown and annealed PbSe thin films

In this case, the PL starts to improve at 275°C and become maximum at 300°C. The results of samples that are annealed at 325°C and 350°C are almost similar and look like PL has become fixed as shown in Fig.3.5. The same trend was observed by Jarod et al. when they heat treated the PbSe sample grown on GaAs substrate at different temperatures from 300°C to 425°C. PL increased from 300°C to 375°C and then decreased significantly at higher temperature (400°C and 425°C) [20]. C.K Bandoh et. al mentioned that at higher temperature (400°C), PbSe deposited on glass substrate starts to evaporate from the surface and affects the quality [21].

Overall, the annealing study resulting the PbSe samples exhibiting a mirror-like grey in color, which remained unchanged after annealing. Additionally, the film adhered well to the glass substrate both before and after the annealing process. The results shows that annealing with nitrogen gas dramatically improves the luminescence around 3.7 μm. The annealing under nitrogen process decreases the trap concentration and altered background career concentration which enhances the electrical and optical

performance of materials and can improved the PL [20].Annealing under nitrogen provides inert environment which limits the loss of selenium and aids in maintaining correct Pb:Se ratio in the nanocrystal film. It also helps in improving interparticle coupling, reducing defects and maintaining surface morphology.

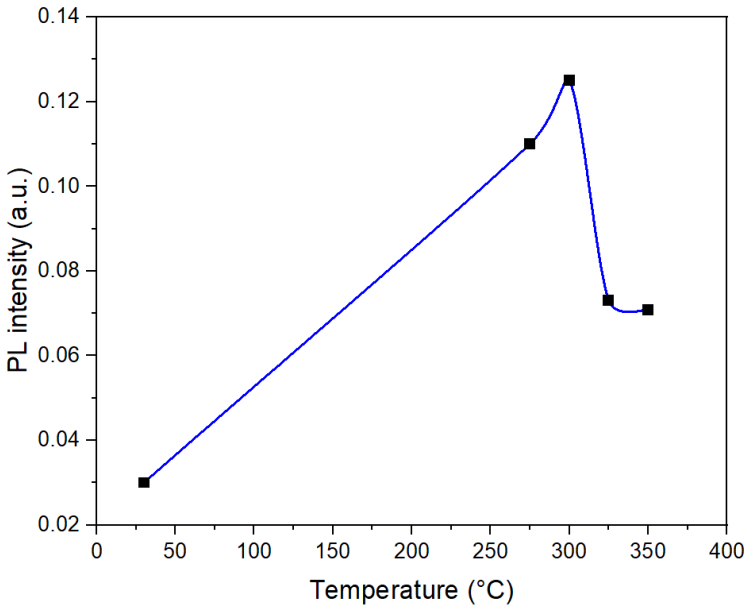

Fig. 3.6: PL signal vs annealed temperature for 30 mins

The Fig.3.6 illustrates the trend of Photoluminescence with respect to temperature. At room temperature, PL was nearly undetectable (0.03 a.u.), it rapidly increases after annealing with temperature 275°C, reached peak at 300°C. At higher temperature 325°C, it sharply decrease and become stable. Through the results, it has been proved that annealing/ heat treatment process plays an important role in improving the photoluminescence of PbSe CBD grown samples.

Besides the PL measurement, the SEM method was conducted using a Zeiss NEON 40EsB Field-Emission SEM with an accelerating voltage of 5 kV. Images were captured at two magnifications: 25,000× and 65,000×. The Fig.3.7 and 3.8 presented below depict the sample before annealing (at room temperature) and after annealing at four different temperatures.

The SEM images after annealing reveal that the nanocrystals remain largely un-

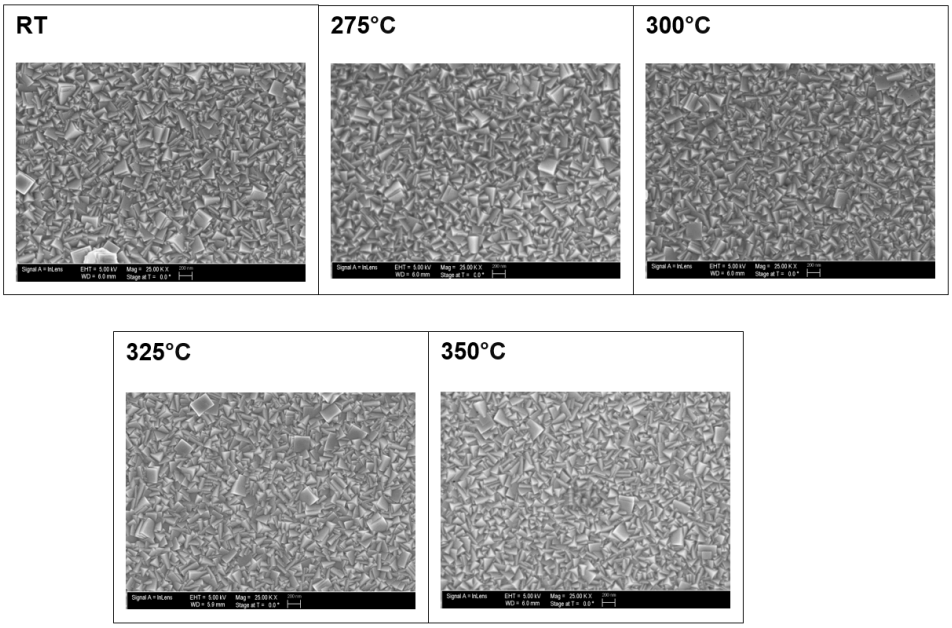

Fig. 3.7: SEM images before annealing (RT) and after annealing at temperature 275°C, 300°C, 325°C, and 350°C

changed, indicating minimal impact on the crystal structure. This suggests that the annealing process does not significantly alter or damage the material's morphology. The annealing with nitrogen gas help reduce non-radiative recombination centers, such as surface defects,or vacancies leading to improved PL without noticeable morphological changes in SEM.

The XRD results shows that peak intensities become less after annealing at 350°C. Moreover, at room temperature peak 220 is dominant while at 350°C, 200 is dominant. Heat treatment can change the orientation and grain size of crystals which changes the peak intensity.

3.3 Conclusion

This study demonstrates that annealing influences the structural and optical properties of PbSe nanocrystals films deposited by the Chemical Bath Deposition (CBD) method.

Annealing under nitrogen gas at moderate temperatures (275-300 °C) enhanced the

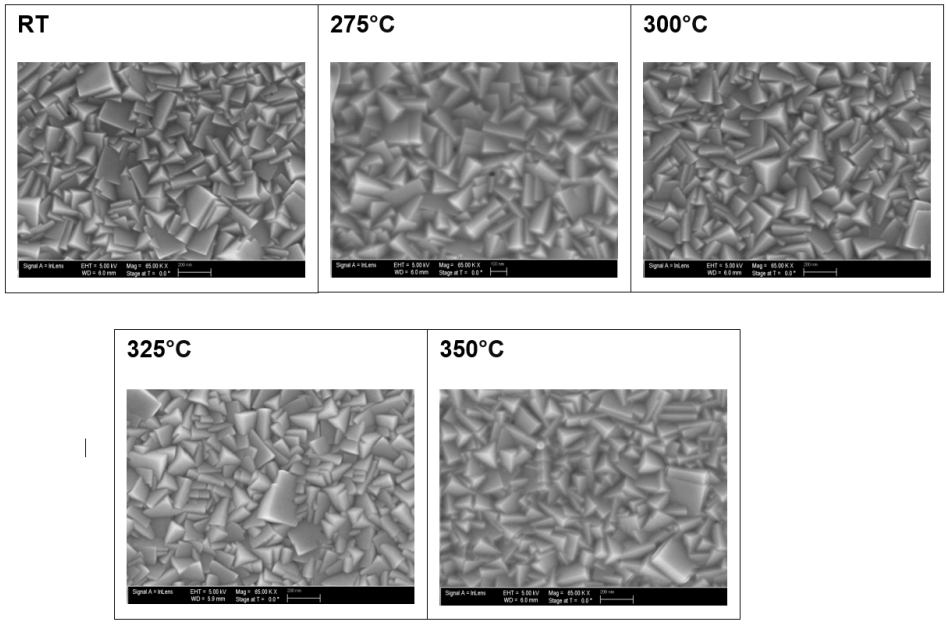

Fig. 3.8: Higher magnification (65000X) SEM images before annealing (RT) and after annealing at temperature 275°C, 300°C, 325°C, and 350°C

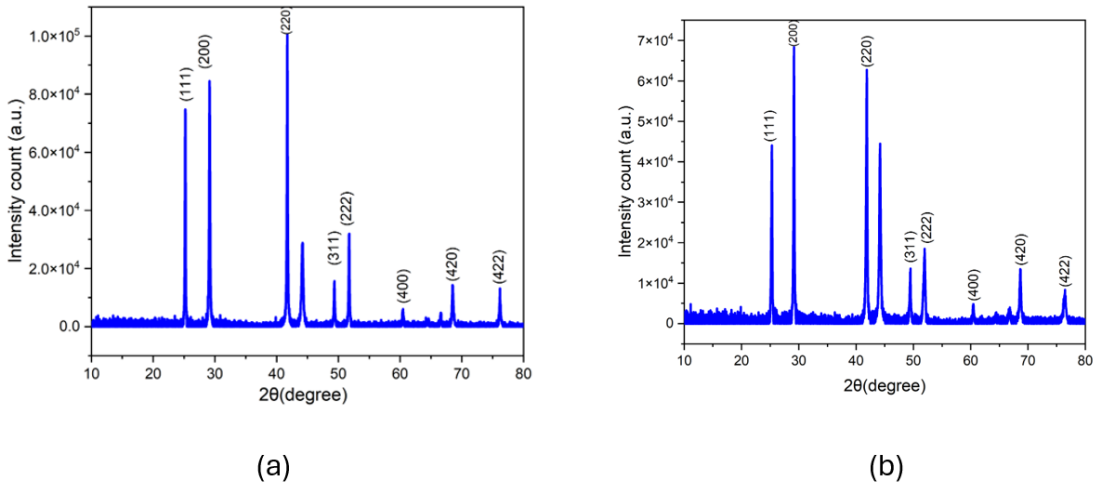

Fig. 3.9: Comparison of XRD of PbSe sample (a) before and (b) after heat treatment at 350°C deposited on Glass substrate

PL intensity, with a maximum observed at 300 °C. This enhancement is attributed to the reduction in non-radiative recombination centers, and modification of carrier concentration. However, further increase in annealing temperature beyond 300 °C led to a decline in PL intensity, possibly due to film degradation, selenium loss, or the crystal defects.

SEM results revealed that morphology of PbSe films remains largely unchanged due to annealing. XRD results showed that reduction in peak intensity after annealing at higher temperature suggesting thermal-induced structural reorientation.

Overall, annealing proves to be an effective post-deposition treatment to optimize the optical performance of PbSe nanocrystal films. Heat treatment under control and inert conditions can enhance their potential for mid-infrared optoelectronic applications.

CHAPTER 4

Photonic Structure Design, Fabrication and Characterization

This chapter presents the simulation, fabrication, and characterization of PbSe-based gratings at the nanoscale. It begins with the simulation of high-contrast gratings, followed by the patterning process using electron beam lithography (EBL). In a subsequent section, I detail the optimization of the Reactive Ion Etching (RIE) method for etching PbSe gratings. Finally, the chapter concludes with post-RIE characterization techniques, including Atomic Force Microscopy (AFM), Scanning Electron Microscopy (SEM), and other relevant analyses. It is highlighted that, despite its simplicity, the HCG structure possesses unique properties and can be used in wide range of fields.

The objective is to make photonic grating design to develop a low-cost mid-infrared light source for gas sensor applications. This new light source based on PbSe films offers a narrow emission bandwidth with a high resonant quality factor which is in favor of selective identification of gases. I target the narrow emission of light at wavelength 3.7um.

The overall process of a gas sensor involves an optical source, a photonic crystal structure, and a photodetector. This work is focused on the photonic crystal structure. A light source is required to put on the grating, and in this case, I used a laser with a wavelength of approximately 980 nm. The grating, composed of lead selenide, is grown using Chemical Bath Deposition (CBD) or a combination of CBD and sputtering, as detailed in Chapter 02.

When the laser light interacts with the grating, it generates a new light source in the mid-infrared region, exhibiting a narrow emission and a high resonant quality factor. My goal was to tune this light source to a wavelength of 3.7 µm, which corresponds

to the absorption characteristics of certain gases. The newly generated light source, after interacting with the gas molecules, is then detected by photo detector, where the resulting electrical signal is measured.

Advanced photonic design provides faster response, higher sensitivity, compact size, low power consumption, and relatively low cost, which are highly desired for modern Internet-of-Things (IoTs) applications.
Photonic-based sensing technologies can be classified into two categories: (1) refractive index-based [23, 24] and (2) absorption-based [25, 26].

Refractive index (RI)-based sensing detects target substances by monitoring changes in the refractive index of the surrounding medium. It operates by measuring shifts in the resonance wavelength caused by variations in the refractive index. Refractive index-based optical sensors include Bloch Surface Wave (BSW) sensors [27], micro-ring resonator sensors [28], and Mach-Zehnder Interferometer (MZI) sensors [29].

In contrast, absorption-based sensing identifies target substances by analyzing their unique absorption spectra at specific wavelengths. It operates by measuring the decrease in light intensity as it passes through the sample, following Beer-Lambert's law. Both of these sensing techniques have broad applications in chemical sensing, medical diagnostics, communication, and energy [30, 31].

Rigorous coupled-wave analysis (RCWA) is a highly accurate and powerful method for analyzing periodic structures, making it essential for the precise design and optimization of photonic devices. RCWA is a widely recognized numerical method for solving Maxwell's equations and analyzing the transmission, reflection, and absorption of waves in a planar grating bounded by two materials with different refractive indices [32]. In RSoft software, this technique is implemented through the Diffract MOD tool.

My numerical design is based on TE-polarized modes, as they offer a significantly

larger spatial coupling volume with gas molecules, potentially enhancing gas sensing performance [33].

4.1 Photonic Grating Design

I designed the simulation in RSoft (DiffractMOD) software to get the emission at wavelength 3.7um. Fig.4.1 illustrate the schematic representation of the HCG, which comprises a PbSe grating layer (nPbSe = 4.9) and a SiO_2 substrate layer (nSiO_2 = 1.4). The key design parameters, including the grating layer thickness (D1), fill factor (F), and grating period (P), are labeled. By optimizing these parameters, the goal is to achieve strong light emission within the grating layer of the HCG.
Previously, Tahere et. al performed simulation of single and couple HCG in combination with absorption based method. The gratings material was Silicon on SiO2 susbstrate, placed under the presence of CO2 gas and found out that CHCG enhance light-gas interaction which has its application in on-chip gas sensing devices [33].

In this simulation design, glass substrate is used on which lead selenide gratings were designed. The assumption made in the simulation is that the glass substrate thickness is infinite.

The key parameters influencing grating design include grating thickness, air gap thickness, fill factor, and period. The thickness of grating (PbSe) is denoted by D1, substrate thickness T, Period P and Fill factor F. The medium around the structure is air (Ref. index=1).

The effective refractive index is a complex function of the local fill factor and often dependent on the polarization of light [34]. The effective refractive index in the TE mode can be find using the following equation.

$$n_{\text{eff}} = \sqrt{n_a^2(1-f)^2 + f \cdot n_g^2} \tag{4.1}$$

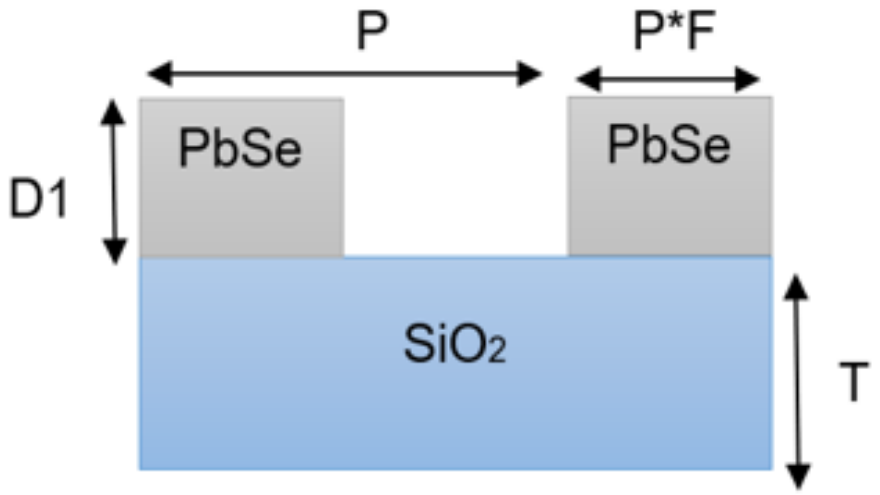

Fig. 4.1: Cross-sectional view of HCG structure design

Where f is fill factor, na and ng are refractive indices of air and grating material (PbSe).

$$\lambda_{\text{res}} = n_{\text{eff}} \cdot P \tag{4.2}$$

The above equation shows that the relation between resonance wavelength and period is linear.

4.2 Simulation Results

To achieve strong light emission at a wavelength of 3.7 µm, the grating parameters of the HCG structure must be carefully modified and optimized. The grating period is one of the key parameters in grating optimization. Based on its value, optical gratings can be classified into three regimes: (1) the diffraction regime, where the period is larger than the wavelength; (2) the deep-subwavelength regime, where the period is significantly smaller than the wavelength; and (3) the near-wavelength regime, where the period is approximately equal to the wavelength [35][36]. I simulated the structure using subwavelength gratings as these gratings show unique optical properties that differ from other diffraction gratings. It was found that when the fill factor (F)

increases, effective refractive index (n.eff) increases as per equation 4.1 and that leads to decrease in period 'P' as per equation 4.2. I optimized the period 'P' and grating thickness 'D1' and found the optimized value to be 1.22 and 0.77 um. I tried simulation with different fill factor ranging from 0.4 to 0.6 and found out that peak shift to higher wavelength with the increase in fill factor.

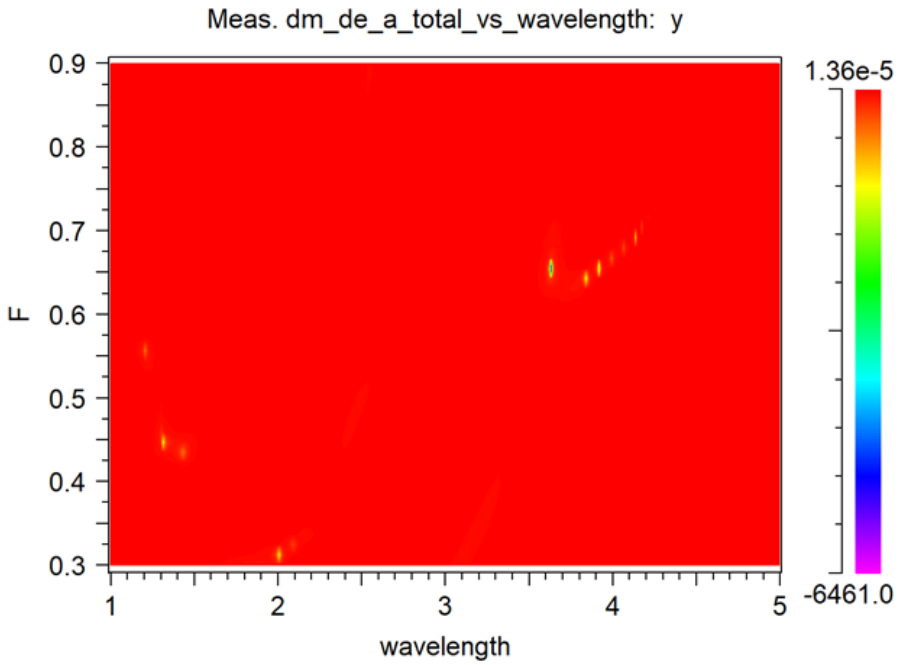

Fig. 4.2: Variation in light absorption achieved by adjusting the fill factor. Optimized fill factor is 0.65 at 3.7um

I optimized the fill factor using the MOST feature of the software and found that a fill factor of 0.65 corresponds to a wavelength around 3.7 µm, shown in Fig.4.2 Through optimization of three different parameters fill factor 'F', period 'P' and grating thickness 'D1', I get narrow emission at 3.7 µm. It is evident that a narrow emission with a high-quality factor can be achieved by optimizing the thickness, grating period and fill factor.

The emission spectra optimized using grating parameters (P = 1.22 µm, F = 0.65, and D1 = 0.77 µm), is presented in Figure 4.3. The highest intensity of the electric field observed is 63.04 $\left(\frac{V}{\mu m}\right)^2$.

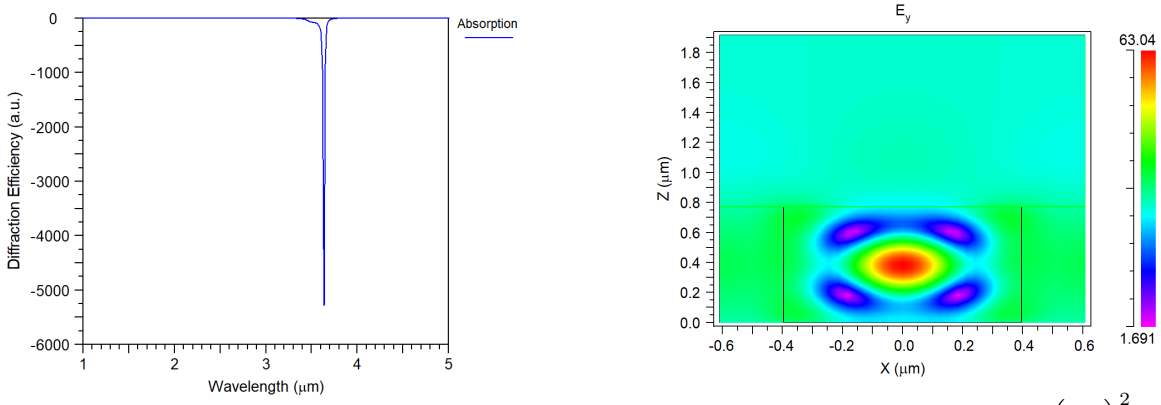

(a) Absorption spectrum peak at 3.7 µm.

(b) Intensity of the electric field $\left(\frac{V}{\mu m}\right)^2$.

Fig. 4.3: (a) Emission spectrum peak observed at 3.7 µm. (b) Colored bar shows the intensity of the electric field $\left(\frac{V}{\mu m}\right)^2$.

The designed grating has a height of 770 nm and a width of 793 nm, resulting in an aspect ratio (height/width) of approximately 1. This low aspect ratio makes fabrication more feasible and less challenging. As the aspect ratio increases, fabrication becomes progressively more difficult[34]. It is worth noting that, although fabricating such a thin substrate is challenging, I utilized advanced current technologies, including EBL and RIE. The results and characterization are presented in following section.

4.3 Fabrication and Characterization Studies

The process flow schematic of PbSe grating fabrication is shown in Fig.4.4
(a) Take Glass substrate, (b) deposit PbSe using CBD method, (c) spin coating of photoresist, (d) after pattern development using EBL, (e) after dry etching (RIE), and (f) final result after removal of resist.

Prior to applying the photoresist, the sample underwent ultrasonic cleaning in acetone for three minutes, followed by another three-minute ultrasonic cleaning in isopropanol (IPA). It was then rinsed with deionized (DI) water and dried using ultra-high purity (UHP) nitrogen gas. E-beam resist PMMA 495K A4 was spin-coated onto the lead selenide sample at a spin rate of 2000 rpm, serving as the resist layer. After PR coating,

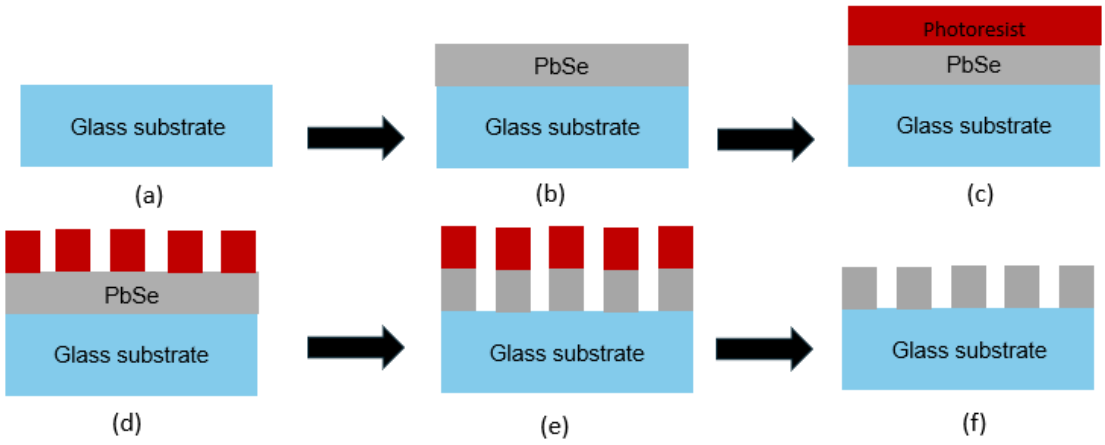

Fig. 4.4: Process flow schematic of PbSe grating fabrication

it was soft baked on hot-plate at 180°C for 90 seconds. A soft bake is performed to eliminate residual solvents from the resist film, essentially drying it out, which improves adhesion to the substrate, prevents sticking to the photomask during exposure, and ensure a stable resist layer. PMMA resist graph in Fig.4.5 shows the relationship between resist thickness and spin speed. As per the graph, around 220nm photoresist is deposited on PbSe sample.

EBL is efficient equipment for fabricating micro and nanostructure patterns. It offers high resolution and is compatible with a wide range of materials [37]. E-beam resist PMMA 495K A4 was used for spin coating. We need high resolution beam to pattern small structure; therefore, we choose small beam current which will have sharper beam head. Beam current range in EBL is from 50pA to 100nA. The minimum time to expose a given area for a given dose is given by the following formula:

$$D \cdot A = T \cdot I \tag{4.3}$$

Where D is the Dose, A is the area exposed, T is the time to expose the object, and I is the beam current.

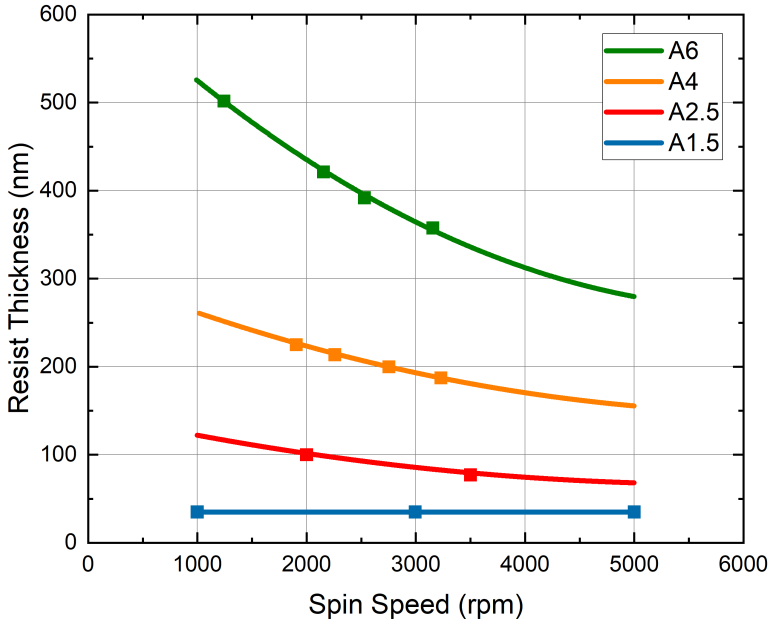

Fig. 4.5: Graph Resist Thickness vs. Spin Speed for different PMMA 495K.

Through E-Beam lithography, a nanometer-scale pattern was exposed on the resist with a beam current of 500 pA and with different dose of 500 to 800 μC/cm^2. Electron beam lithography (EBL) was used to pattern the same design on PbSe deposited on both glass and silicon substrates.

The acceleration voltage used was 125kV. Typically, Electron Beam Lithography (EBL) is conducted at a high acceleration voltage, allowing the electron beam to be further focused using external electromagnetic fields. This process minimizes the spot size to the 10-nm level without requiring additional steps [38].

The development of exposed resist was performed using a 3:1 solution of methyl isobutyl ketone (MIBK) and isopropyl alcohol for 90 seconds, followed by a 10-second rinse in isopropyl alcohol, and then blow-dried using pure nitrogen gas.

The SEM images captured shown in Fig.4.6 and 4.7 after development indicate that at doses of 500 and 600 μC/cm^2, the contrast is challenging to distinguish. This suggests

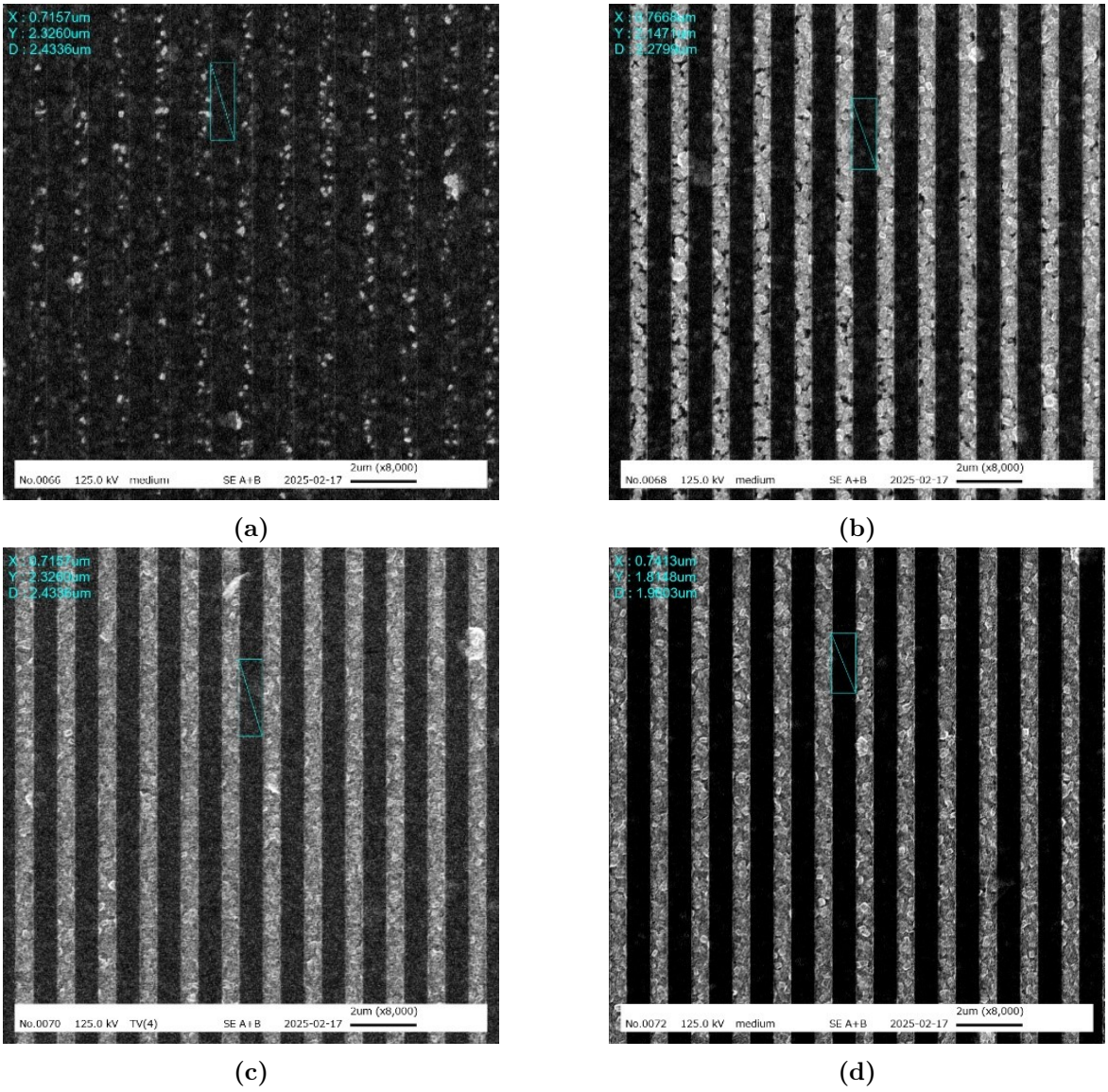

Fig. 4.6: Comparison of SEM images of PbSe deposited on glass having patterning with different doses (a)500 μC/cm^2, (b)600 μC/cm^2, (c)700 μC/cm^2, and (d)800 μC/cm^2.

potential underexposure caused by the proximity effect, where electron scattering in the e-beam resist and substrate leads to a broader exposure area, ultimately limiting resolution [39]. In contrast, the exposure results are significantly improved at doses of 700 and 800 μC/cm^2, indicating optimal exposure conditions for improved pattern resolution.

There are two types of etching process used in micro-fabrication for removal of material i.e (wet and dry etching). Wet etching is a simple and cost effective method, but it is

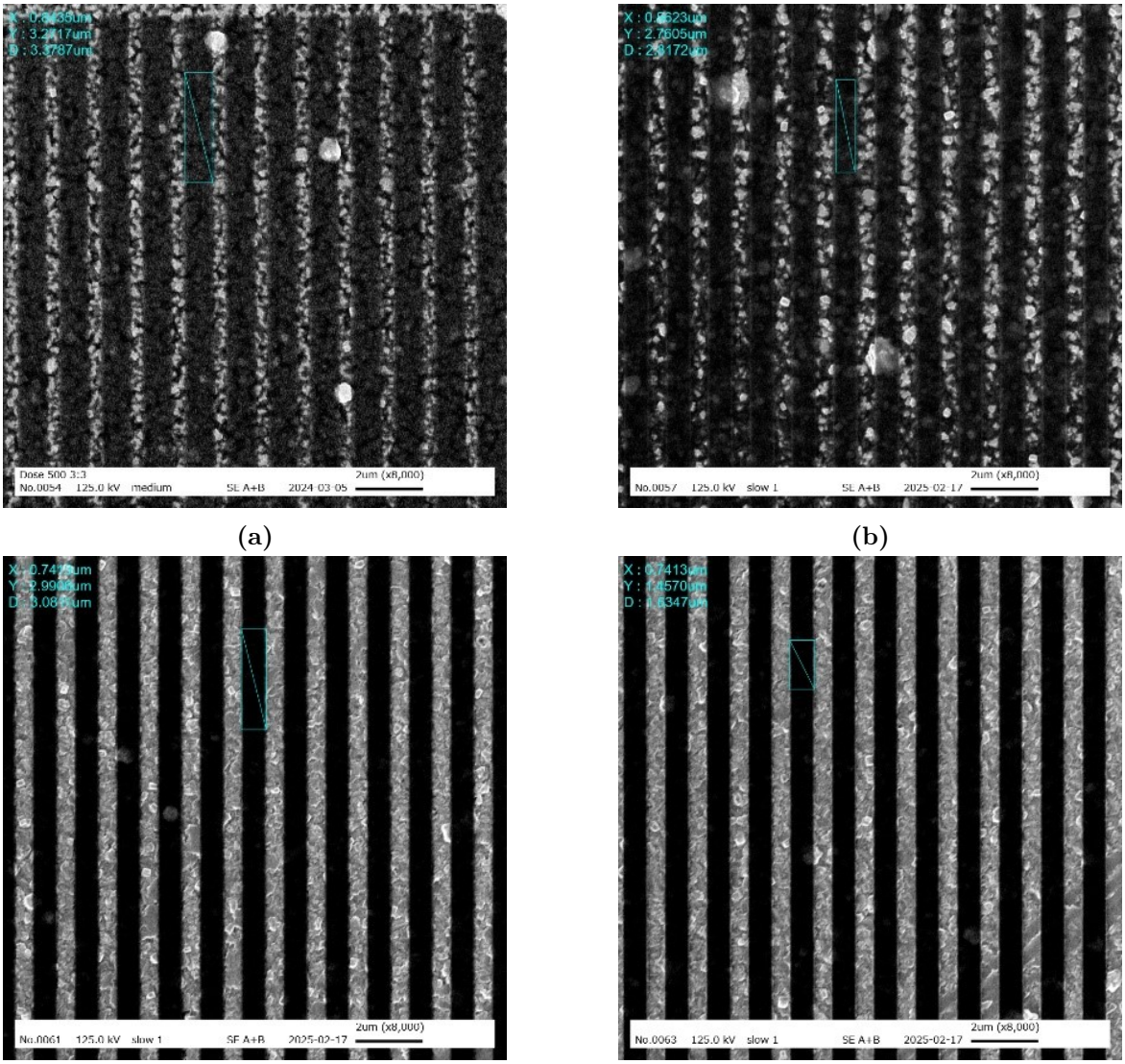

Fig. 4.7: Comparison of SEM images of PbSe deposited on silicon having patterning with different doses (a)500 μC/cm^2, (b)600 μC/cm^2, (c)700 μC/cm^2, and (d)800 μC/cm^2.

difficult to control precision for small-scale features and has potential for undercutting in isotropic etching. Dry etching includes Reactive Ion Etching (RIE), which is a plasma-based dry etching technique commonly used in micro fabrication. It enables precise and anisotropic material removal by using chemically reactive ions accelerated towards the substrate which was desirable in my experiment. To determine the etch rate, a PbSe sample deposited via sputtering was used. The initial thickness was measured to be 330 nm. Reactive ion etching (RIE) was performed at two different

chamber temperatures, 30°C and 50°C, for a duration of three minutes. To ensure selective etching, the sample was partially covered with tape, exposing only a small area.

At 30°C, the uncovered PbSe was completely etched within three minutes, indicating an etch rate exceeding 110 nm/min. However, since the PbSe layer was fully removed, the exact etch rate could not be accurately determined, making the surface transparent. In contrast, at 50°C, the exposed PbSe did not fully etch away and instead darkened. Profilometer measurements showed that only 58 nm of material was removed, corresponding to a significantly slower etch rate of approximately 19 nm/min.

These findings suggest that as the chamber temperature increases, the etch rate decreases, and the etching quality deteriorates, leading to surface darkening.
It is important to note that the use of Kapton tape to cover the PbSe sample negatively impacts the etching process, leading to poor etching results. The observations indicate that during tape removal after etching, PbSe occasionally peels off along with the tape. Additionally, exposure to plasma causes the tape to release residues and byproducts, leading to contamination, especially at higher temperatures.

Furthermore, if etching is performed on a PbSe surface previously covered by the tape, the residual adhesive alters the etching rate due to its interaction with the material. To avoid these issues, I decided not to use Kapton tape for masking in future etching processes. To optimize the etching process, a more detailed study was carried out using five different temperatures, ranging from 15°C to 35°C in increments of 5°C and etched for a duration of only one minute.

I investigated the effect of reactor chamber temperature on the etching rate. Initially, I etched the PbSe sample at 15°C, 25°C, and 35°C and measured the thickness using a profilometer. The measurements showed etching rates of 105, 155, and 130 nm/min,

respectively, indicating that the highest etching rate occurred at 25°C.

Fig. 4.8: Cleaning of Reactive Ion Etching reactor chamber

However, an unexpected issue arose when I etched at a higher temperature of 45°C and then attempted to repeat the etching process at 25°C. The surfaces of both samples became contaminated, and profilometer measurements showed no noticeable thickness differences. The most probable cause of this issue was contamination within the reactor chamber.

To resolve this, I thoroughly cleaned the chamber, as shown in the figure 4.8, and repeated the etching process at temperature 25°C and 30°C. The etching rates were found to be 148 nm/min and 129 nm/min, respectively, after measurement with profilometer. The Fig.4.9 displays the effect of chamber temperature on etch rate and optimized etch rate observed at temperature 25°C.

Finally, I etched my patterned sample at temperature 25°C for five minutes. The AFM results show that the unwanted PbSe was not completely etched away and only 400 nm is etched. To remove the photoresist after RIE, the sample was first immersed in acetone for three minutes, followed by rinsing in IPA and DI water for one minute each. The sample was then dried using a nitrogen gas. To eliminate any remaining residues, a plasma asher was used with a power setting of 50W at 200mTorr for three minutes.

The etch rate of a PbSe sample without grating was determined to be 148 nm/min

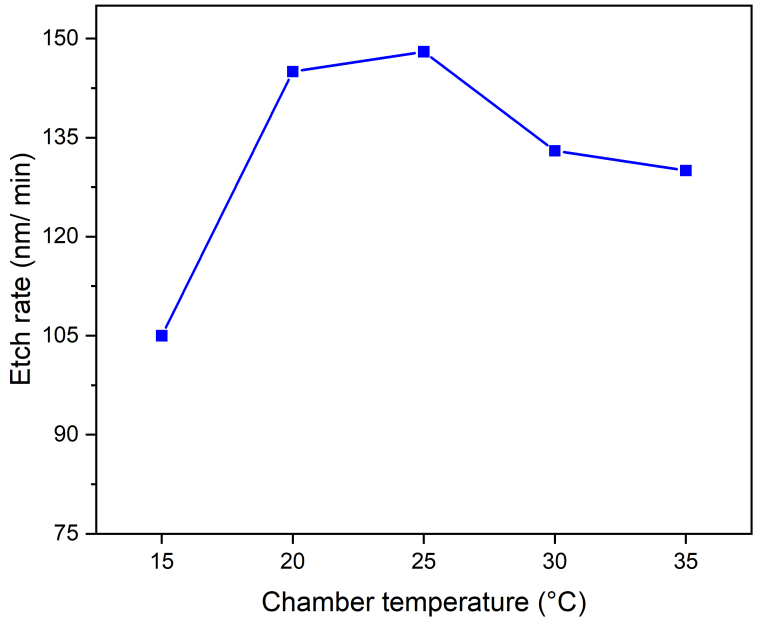

Fig. 4.9: Effect of chamber temperature on etch rate

at a chamber temperature of 25°C. AFM images as shown in Fig.4.10 and 4.11 were taken after etching PbSe with gratings revealed that only 400 nm was removed for dose 700 μC/cm^2 instead of the expected 750 nm within five minutes.

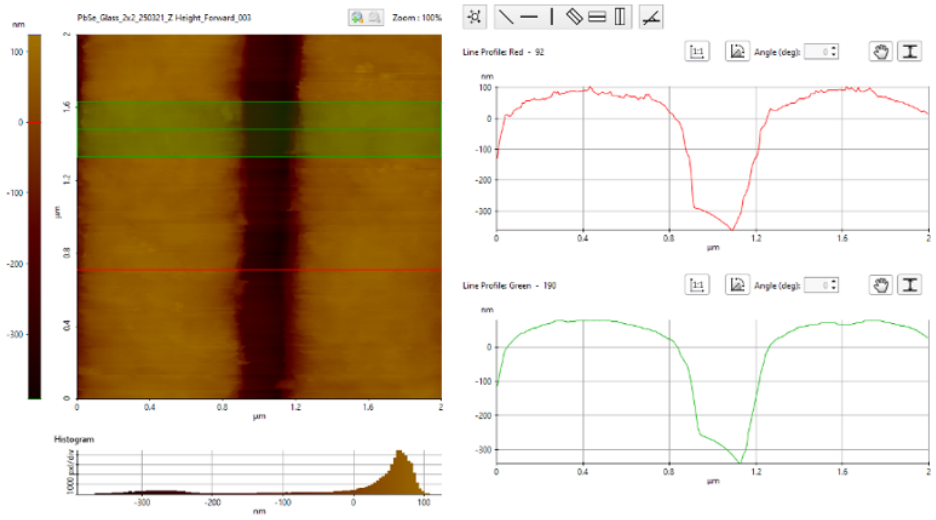

Fig. 4.10: AFM image after etching

The incomplete etching is likely due to the narrow spacing (on the nanometer scale) be-

tween the gratings, which requires a longer etching duration. Smaller feature sizes can restrict the flow of ions, leading to a slower etching rate. Furthermore, during plasma etching, the accumulation of charges in narrow trenches can deflect ions, reducing the efficiency of the etching within the grating spaces.

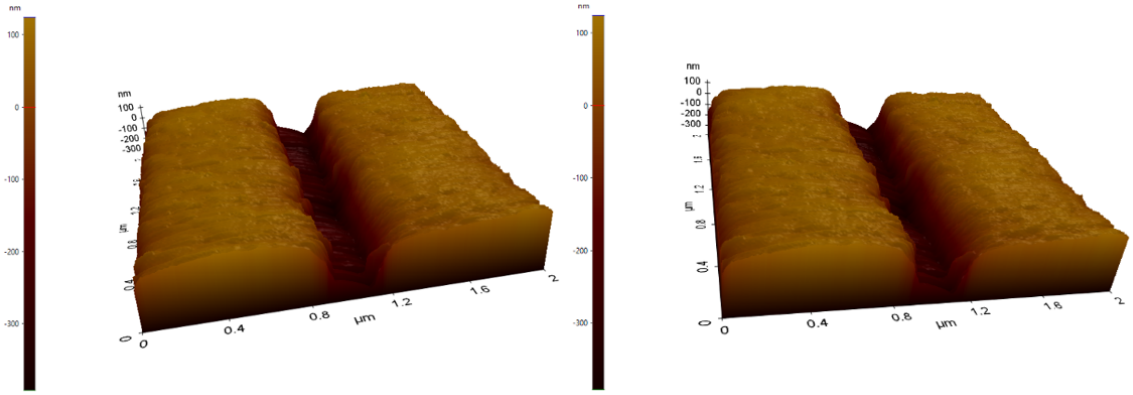

Fig. 4.11: AFM 3D images after etching

I used a cryogenic dewar to study PL at different temperatures with a Calcium Fluoride window. Calcium Fluoride (CaF_2) is a highly transparent material with a low absorption coefficient, making it ideal for applications requiring high transmission across a broad wavelength range, from the ultraviolet (180 nm) to the infrared (8 μm).

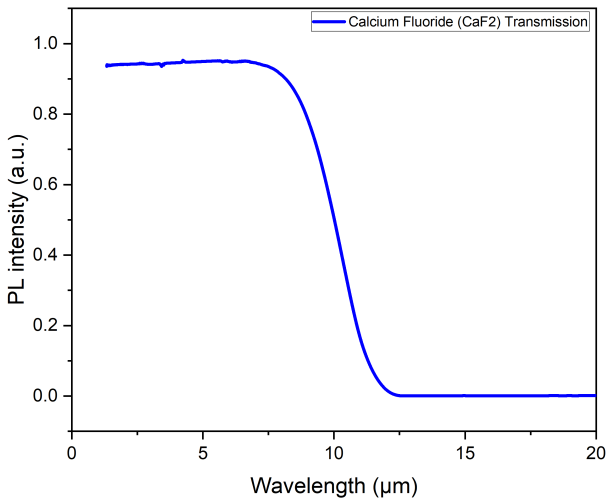

Fig. 4.12: Transmission of Calcium Fluoride

To verify the presence of a calcium fluoride window in the cryogenic system, I con-

ducted a transmission analysis of the material. The resulting spectrum confirmed its optical properties, providing clear evidence that the material is indeed CaF_2, as shown in Fig.4.12.

After placing the sample in the cryogenic sample holder, the vacuum pressure was maintained at 6×10^{-6} torr using the turbo molecular pump, as shown in Fig.4.13.

Fig. 4.13: Turbomolecular pump used to achieve vacuum in cryogenic at lower pressures

Fig.4.14 displays PL intensity increases as the current increases from 900mA to 2000mA. It means higher current injection leads to stronger photo luminesce due to electron-hole recombination. At lower temperatures (e.g., 80K, 120K), the PL intensity continues to increase with current and at higher temperatures (e.g., 240K, 280K), PL intensity initially rises but then tends to saturate beyond around 1400mA. It may be associated to increased non-radiative recombination processes at higher temperatures. For higher temperatures (240K and 280K), the PL intensity appears to be constant beyond a certain current (1400 mA), indicating a possible efficiency droop due to thermal effects.

Fig.4.15 displays images of various patterns obtained after reactive ion etching (RIE) and resist removal, captured using a Thorlabs camera connected to an FTIR system.

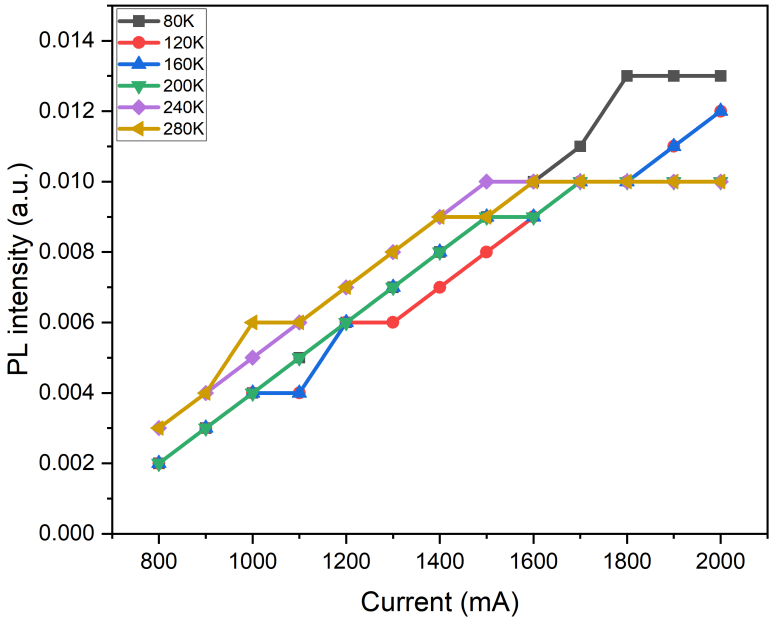

Fig. 4.14: Effect of change in current on PL intensity at different temperatures on PbSe samlple (outside the gratings)

On the graph (Fig.4.16),effect of change in current on PL intensity at different temperatures on gratings is displayed. The X-axis represents the applied current ranging from approximately 800 mA to 2000 mA. The Y-axis (PL Intensity in Arbitrary Units - a.u.) represents the Photoluminescence (PL) intensity, which is an indicator of light emission. Different colored markers represent various temperatures (80K to 300K).

Different temperatures were maintained inside the cryogenic system using the Cryogenic Temperature Controller Model 325, ranging from 77K to 300K with a step size of 40K. Photoluminescence (PL) measurements were conducted at various currents, from 800 mA to 2000 mA (laser power from 1.52 to 4.26 Watts) , with a step size of 100 mA, across different temperatures.

The Fig. 4.16 demonstrates a linear response at lower temperatures. However, as the temperature increases, the curve saturates more quickly than at lower temperatures. At higher temperatures, PL intensity declines at higher currents, leading to efficiency

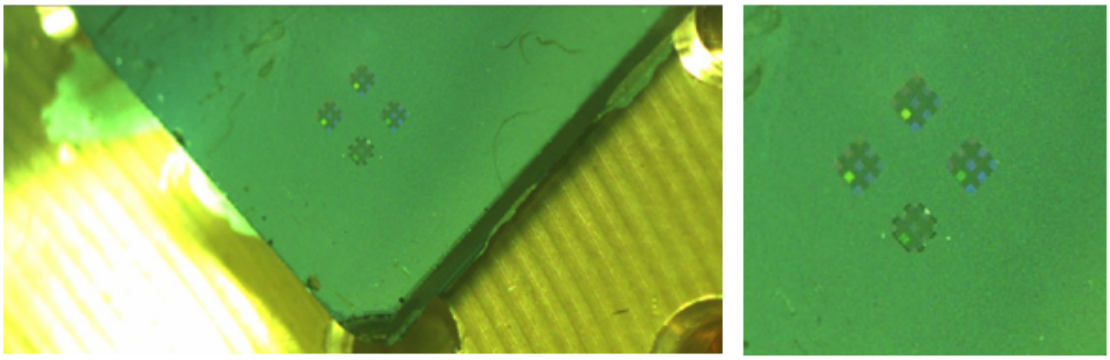

Fig. 4.15: Pattern after etching on PbSe sample with four different doses 400 to 800 $\mu C/cm^2$

loss, most likely due to non-radiative recombination. In this process, electrons and holes recombine, releasing energy in the form of heat instead of photon emission. This results in reduced light emission and increased heat generation, which is undesirable.

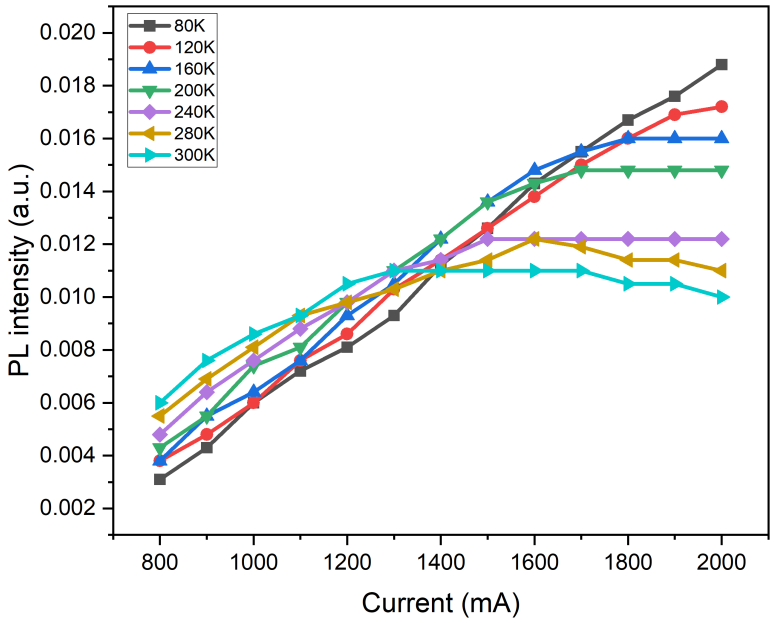

Fig. 4.16: Effect of change in current on PL intensity at different temperatures on gratings

Conversely, at lower temperatures, PL intensity continues to rise with increasing current, indicating efficient radiative recombination, where electrons and holes recombine to release photons as light. The graph also reveals that beyond a certain current level (1600–1800 mA), PL intensity saturates or even decreases at higher temperatures (e.g.,

240K, 280K, and 300K). This behavior is likely caused by non-radiative recombination, which becomes dominant at higher currents, suppressing light emission.

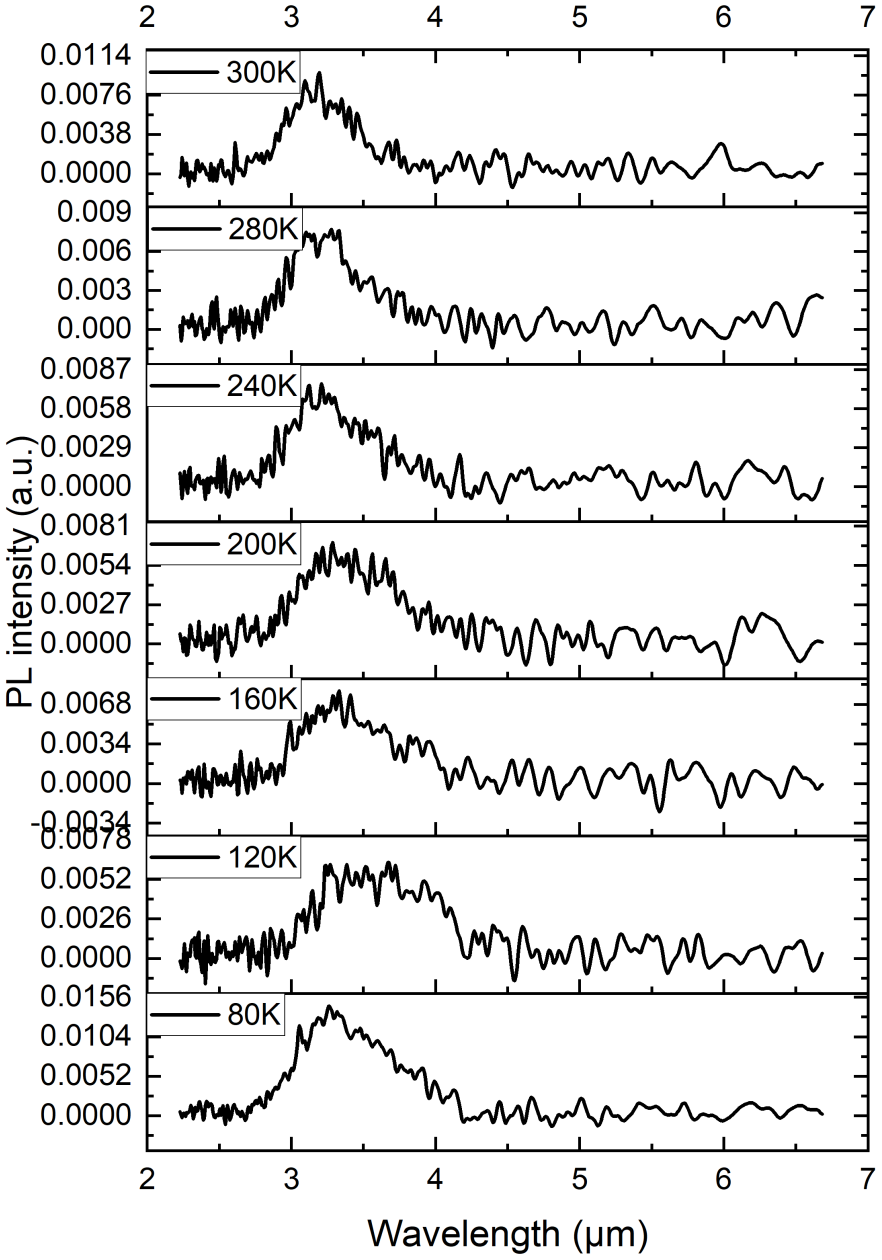

Fig. 4.17: PL spectrum observed at different temperature on grating at currennt 1000mA

The Fig.4.17 shows the PL spectra of grating sample using FTIR at various temperatures (from 80K to 300K). A excitation power remains the same by maintaining constant current of 1000mA across all measurements. It has been observed that as

the temperature decreases, the PL intensity increases in the range of 3 to 4um due to electron-hole recombination. The peak position slightly blueshifts and become sharper at lower temperature indicating narrow linewidths due to reduced thermal broadening and bandgap widens with cooling. Overall, lowering the temperature enhances the PL intensity and sharpen the spectra due improved radiative efficiency and reduced thermal quenching at low temperatures.

The table 4.1 illustrates the comparison of roughness before and after the fabrication process, where Rq is the root-mean-squared (RMS) roughness and Ra is the average roughness. It has been observed that both Rq and Ra of the PbSe thin film increased after the patterning and etching processes. This enhancement in surface roughness plays a significant role in improving light extraction efficiency compared to that achieved with the flat, unprocessed surface of the material.

Table 4.1: Comparison of Surface roughness of PbSe samples.

Sample	Min(nm)	Max(nm)	Mid(nm)	Rq	Ra
PbSe on Glass sample	-126.54	131.59	2.525	32.29	25.90
PbSe sample (After etching)	-342.33	80.27	-131.03	120.73	89.95

The primary reason for this improvement is the reduction in total internal reflection at the interface between PbSe and air. PbSe is a high-refractive-index material, and when light attempts to transition from PbSe to air, a flat surface causes a strong refractive index mismatch. This mismatch results in a considerable portion of the light being reflected back into the material rather than escaping. However, a rough surface disrupts this effect by introducing random micro- and nano-scale features that scatter light in various directions. This angular scattering lowers the probability of light being reflected back into the material, thereby increasing the chances of photon escape.

Moreover, the roughened surface acts as a form of an anti-reflective structure. It provides a more gradual transition in refractive index from the PbSe film to air, effectively

reducing Fresnel reflection losses. This graded-index effect allows more light to pass through the interface rather than being reflected. As a result, the overall internal optical losses are minimized.

In addition to enhanced light extraction, the increase in surface roughness also improves light-matter interaction by extending the optical path length within the material. This can be particularly advantageous in applications such as photodetectors or optoelectronic devices, where increased interaction time leads to better performance.

Overall, the introduction of surface roughness through patterning and etching enhances the optical properties of PbSe thin films by improving light outcoupling, reducing reflective losses, and enabling more efficient device operation.

4.4 Conclusion

This chapter presents the simulation and fabrication of a narrowband emitter using a high-contrast grating (HCG). The fabrication process includes resist coating, patterning via electron beam lithography (EBL), and etching to remove unwanted PbSe. Characterization was conducted using the AFM to measure etching depth and surface roughness, while FTIR was used to analyze photoluminescence (PL) both within and outside the patterned region at different currents and temperatures. The results confirm that the emission was successfully enhanced by implementing the simulated design in fabrication. Our proposed photonic crystal grating structures, developed as a light source, demonstrate strong potential for toxic chemical and gas detection, making them highly valuable for industrial safety applications.

CHAPTER 5

Research Summary and Future Scope

The Mid-IR spectrum features strong absorption bands of chemical molecules and two atmospheric windows, serving a wide range of applications, including gas sensing, thermal imaging, and free space optical communication. In this thesis, I have conducted the experimental studies on synthesizing PbSe materials using a modified CBD method developed by our research group, as well as the photonic design and structure fabrication to investigate its potential for making the mid-IR light emitting devices.

I started the work from the background review study to understand the fundamental characteristics of PbSe, as presented in Chapter one. From which, I learn that PbSe is a direct bandgap semiconductor with a narrow bandgap of 0.27 eV at room temperature, making it an excellent candidate for mid-IR detection. PbSe also exhibits low Auger recombination rates, which contribute to higher sensitivity in mid-IR devices such as detectors and emitters. The chapter also explains the principles and advantages of High Contrast Gratings (HCGs), a promising photonic structure for achieving low-cost, low-power-consumption mid-IR emitters. These features are particularly beneficial for compact and efficient gas-sensing devices.Furthermore, I also reviewed various methods for PbSe thin film growth, with a focus on the Chemical Bath Deposition (CBD) technique. The advantages and limitations of CBD are discussed, along with comparisons to other chemical methods such as Ion-by-Ion (IBI), Oriented Attachment (OA), and cluster-based growth. Special emphasis is placed on the OA method due to its potential to form well-aligned nanocrystals with improved optical properties.

With the support of the accumulated background knowledge, I started my experimental effort to make myself able to repeatably grow the PbSe high quality thin films via the oriented growth method that was initially developed my Dr. Tahere Hemati who had graduated in our group. The growth mechanism was investigated using the oriented attachment CBD method. PbSe thin films were grown using two different approaches: the hot plate method and the water bath method. It was observed that the water bath method produced more uniform and controlled film growth. Various parameters such as pH, temperature, and growth time were systematically varied to study their impact on PbSe deposition. Lower temperatures led to cluster-like growth due to reduced solubility, while higher temperatures favored larger crystal formation. Increasing the volume of water reduced the OH^- concentration, resulting in larger cubic crystals with more spacing between them, indicative of an ion-by-ion growth mechanism. The NaOH concentration also significantly influenced film quality; higher OH^- concentrations produced undesirable highly transparent films. Optimized values of water volume, temperature, and NaOH concentration were identified and used for film growth. Both single-layer and double-layer CBD growths were carried out, and film thickness and photoluminescence (PL) were measured after each layer. A significant enhancement in PL was observed after the double-layer deposition. Additionally, growth was performed on both glass and silicon substrates using a sputtered seed layer to support CBD. The resulting films were analyzed using SEM, XRD, and PL to evaluate and compare material properties across the different growth conditions and substrate types.

Following the growth, I conducted the study of the post annealing method in order to enhance the optical properties of PbSe thin films. Annealing was carried out in a split tube furnace under nitrogen gas at temperatures ranging from 275 °C to 350 °C for 30 minutes. Photoluminescence (PL) measurements revealed that the PL intensity began to increase at 275 °C, peaked at 325 °C, and declined at the higher temperature

of 350 °C. Post-annealing characterization, including SEM and XRD analysis, was conducted. SEM images indicated minimal changes in crystal size, and no noticeable change in the sample's color was observed after annealing.

Having the ability to prepare material and enhance its quality, I then move to the next step to perform the simulation, fabrication, and characterization works for making a photonic grating designed for narrowband light emission centered around 3.7 μm with a high Q-factor. The High Contrast Grating (HCG) structure was designed using RSoft's DiffractMOD simulation software with subwavelength grating features. The optimized grating parameters were found to be: period = 1.22 μm, fill factor = 0.65, and grating thickness = 770 nm. The fabrication process involved photolithography, starting with spin-coating a layer of PMMA 495K A4 photoresist on the PbSe substrate. Due to the submicron feature size of the design (below 1 μm), Electron Beam Lithography (EBL) was employed instead of a mask aligner, which is limited to resolutions above 1 μm. Various exposure doses ranging from 500 to 800 μC/cm^2 were tested. SEM imaging revealed that doses between 500–600 μC/cm^2 led to underexposed patterns, while doses in the 700–800 μC/cm^2 range produced well-defined gratings. Following development, Reactive Ion Etching (RIE) was used to transfer the pattern. Challenges arose during the RIE process in determining an accurate etch rate across different reactor chamber temperatures. Multiple analyses revealed that thorough chamber cleaning significantly influenced the consistency of etch rates. The optimal chamber temperature for etching was found to be 25 °C, which was subsequently used for etching the patterned samples. For structural characterization, Atomic Force Microscopy (AFM) was performed to evaluate the etch depth and surface roughness. Complete etching was not achieved within the estimated time, likely due to the nanoscale dimensions of the grating, which slowed the etching process.For optical characterization, photoluminescence (PL) measurements were performed on both patterned and unpatterned regions. The sample was mounted inside a cryogenic chamber, and vacuum was created using a turbo-

molecular pump. PL measurements were taken across a temperature range from 80 K to 300 K in 40 K increments. Laser currents ranging from 900 mA to 2000 mA were used for excitation. The PL intensity was observed to increase with current at lower temperatures, indicating efficient radiative recombination. However, at higher temperatures, PL intensity saturated or even decreased beyond a certain current threshold (1600–1800 mA), likely due to non-radiative recombination processes. Furthermore, at elevated temperatures, the PL curve reached saturation more rapidly, indicating reduced emission efficiency compared to lower temperatures.

Lastly, to conclude, the studies on PbSe thin films and HCGs for mid-IR applications have several avenues for continuous future exploration. Building on the modified CBD method and photonic design, subsequent work could focus on scaling the synthesis process to achieve larger-area, defect-free PbSe films for commercial-grade mid-IR emitters and detectors. Further refinement of HCG parameters, such as exploring the optimized structure etching as well as parity-time asymmetric, hybrid or multi-layer gratings, could enhance Q-factor and emission efficiency, targeting specific wavelengths for advanced gas sensing or optical communication. Additionally, integrating these devices with on-chip electronics or microfluidic systems could enable portable, real-time environmental monitoring platforms. Investigating alternative substrates, treatment or fabrication strategies to boost photoluminescence performance and stability at higher temperatures will also be critical for practical deployment. Overall speaking, these advancements promise to strengthen the role of PbSe-based photonics in addressing pressing needs in industrial, defense, and healthcare applications.

List of Abbreviations

PbSe	Lead Selenide
MIR	Mid Infrared
NIR	Near Infrared
CBD	Chemical Bath Deposition
DL	Double Layer
PL	Photoluminescence
PR	Photoresist
PMMA	Polymethyl Methacrylate
EBL	Electron Beam Lithography
RIE	Reactive Ion Etching
LPM	Liter Per Minute
RT	Room Temperature
SEM	Scanning Electron Microscopy
XRD	X-ray Diffraction
AFM	Atomic Force Microscopy
FTIR	Fourier Transform Infrared Spectroscopy
HCG	High Contrast Grating
Rq	Root Mean Square Roughness
Ra	Average Roughness
μm	Micrometer
nm	Nanometer

List of Key Symbols

Bibliography

[1] J. R. Meyer, C. L. Canedy, M. Kim, C. S. Kim, C. D. Merritt, W. W. Bewley, and I. Vurgaftman, "Comparison of auger coefficients in type i and type ii quantum well midwave infrared lasers," *IEEE Journal of Quantum Electronics*, vol. 57, no. 5, pp. 1–10, 2021.

[2] T. Hemati, X. Zhang, and B. Weng, "A direct oriented-attachment growth of lead-chalcogenide mid-infrared nanocrystals film on amorphous substrates," *Journal of Materials Chemistry C*, vol. 8, no. 38, pp. 13 205–13 212, 2020.

[3] D. Popa and F. Udrea, "Towards integrated mid-infrared gas sensors," *Sensors*, vol. 19, no. 9, p. 2076, 2019.

[4] Á. I. López-Lorente and B. Mizaikoff, "Mid-infrared spectroscopy for protein analysis: potential and challenges," *Analytical and bioanalytical chemistry*, vol. 408, pp. 2875–2889, 2016.

[5] J. Park, M. M. Al Mahfuz, R. Huebner, and D.-K. Ko, "Uncooled mid-wavelength infrared photoconductive detectors based on pbse nanocrystals," *ACS Applied Electronic Materials*, vol. 5, no. 4, pp. 2386–2393, 2023.

[6] J. Emerson-Reynolds, "Xxv.—on the synthesis of galena by means of thiocarbamide, and the deposition of lead sulphide as a specular film," *Journal of the Chemical Society, Transactions*, vol. 45, pp. 162–165, 1884.

[7] J. Qiu, B. Weng, L. Li, X. Li, and Z. Shi, "Large-scale self-assembled epitaxial growth of highly-ordered three-dimensional micro/nano single-crystalline pbse pyramid arrays by selective chemical bath deposition," *Materials Research Express*, vol. 2, no. 5, p. 055010, 2015.

[8] R. Schwanninger, S. M. Koepfli, O. Yarema, A. Dorodnyy, M. Yarema, A. Moser, S. Nashashibi, Y. Fedoryshyn, V. Wood, and J. Leuthold, "Highly responsive mid-infrared metamaterial enhanced heterostructure photodetector formed out of sintered pbse/pbs colloidal quantum dots," *ACS Applied Materials & Interfaces*, vol. 15, no. 8, pp. 10 847–10 857, 2023.

[9] M. C. Gupta, J. T. Harrison, and M. T. Islam, "Photoconductive pbse thin films for infrared imaging," *Materials Advances*, vol. 2, no. 10, pp. 3133–3160, 2021.

[10] S. Gorer, A. Albu-Yaron, and G. Hodes, "Chemical solution deposition of lead selenide films: a mechanistic and structural study," *Chemistry of materials*, vol. 7, no. 6, pp. 1243–1256, 1995.

[11] T. Templeman, S. Sengupta, N. Maman, E. Bar-Or, M. Shandalov, V. Ezersky, E. Yahel, G. Sarusi, I. Visoly-Fisher, and Y. Golan, "Oriented attachment: a path to columnar morphology in chemical bath deposited pbse thin films," *Crystal Growth & Design*, vol. 18, no. 2, pp. 1227–1235, 2018.

[12] Y. Liu, L. L. McDowell, L. Su, Y. Luo, J. Qiu, and Z. Shi, "Morphological and microstructural evolution of high-quality pbse epitaxial film on si substrate by chemical bath deposition," *Materials Science in Semiconductor Processing*, vol. 150, p. 106963, 2022.

[13] A. Bhardwaj, P. Srivastava, and H. Sehgal, "Chemically deposited pbse nanoparticle films: Variation in shape and size," *Journal of The Electrochemical Society*, vol. 154, no. 10, p. K83, 2007.

[14] M. Shandalov and Y. Golan, "Microstructure and morphology evolution in chemical solution deposited pbse films on gaas (100)," *The European Physical Journal-Applied Physics*, vol. 24, no. 1, pp. 13–20, 2003.

[15] P. Fallah Azad, N. Naderi, M. J. Eshraghi, and A. Massoudi, "The effect of seed layer on optical and structural characteristics of zno nanorod arrays deposited by cbd method," *Journal of Materials Science: Materials in Electronics*, vol. 28, pp. 15 495–15 499, 2017.

[16] S. Thanikaikarasan, T. Mahalingam, V. Dhanasekaran, A. Kathalingam, and J.-K. Rhee, "Growth and characterization of lead selenide thin films," *Journal of Materials Science: Materials in Electronics*, vol. 23, pp. 1562–1568, 2012.

[17] F. Zhao, S. Mukherjee, J. Ma, D. Li, S. Elizondo, and Z. Shi, "Influence of oxygen passivation on optical properties of pbse thin films," *Applied Physics Letters*, vol. 92, no. 21, 2008.

[18] J. Qiu, B. Weng, Z. Yuan, and Z. Shi, "Study of sensitization process on mid-infrared uncooled pbse photoconductive detectors leads to high detectivity," *Journal of applied physics*, vol. 113, no. 10, 2013.

[19] N. Tret'yakova, "Study of heat-sensitization modes of lead selenide films prepared

by hydrochemical synthesis," *Journal of Surface Investigation. X-ray, Synchrotron and Neutron Techniques*, vol. 8, no. 4, pp. 632–635, 2014.

[20] J. E. Meyer, L. Nordin, T. Nguyen, and K. Mukherjee, "Mid-wave infrared photoluminescence from low-temperature-grown pbse epitaxial films on gaas after rapid thermal annealing," *Applied Physics Letters*, vol. 123, no. 13, 2023.

[21] C. Bandoh, I. Nkrumah, F. Ampong, R. Nkum, and F. Boakye, "Effect of annealing on the structure and optical properties of lead selenide and cadmium selenide thin film prepared by chemical bath deposition." *Chalcogenide Letters*, vol. 18, no. 2, 2021.

[22] M. H. Kabir, M. M. Ali, M. A. Kaiyum, and M. Rahman, "Effect of annealing temperature on structural morphological and optical properties of spray pyrolized al-doped zno thin films," *Journal of Physics Communications*, vol. 3, no. 10, p. 105007, 2019.

[23] M. Quan, J. Tian, and Y. Yao, "Ultra-high sensitivity fabry–perot interferometer gas refractive index fiber sensor based on photonic crystal fiber and vernier effect," *Optics letters*, vol. 40, no. 21, pp. 4891–4894, 2015.

[24] N. Ayyanar, G. T. Raja, M. Sharma, and D. S. Kumar, "Photonic crystal fiber-based refractive index sensor for early detection of cancer," *IEEE sensors journal*, vol. 18, no. 17, pp. 7093–7099, 2018.

[25] X. Yu, Y. Zhang, Y. C. Kwok, and P. Shum, "Highly sensitive photonic crystal fiber based absorption spectroscopy," *Sensors and Actuators B: Chemical*, vol. 145, no. 1, pp. 110–113, 2010.

[26] J. Wang and L. Wang, "Carbon dioxide gas sensor derived from a 547-hole microstructured polymer optical fiber preform," *Optics letters*, vol. 35, no. 19, pp. 3270–3272, 2010.

[27] W. Kong, Z. Zheng, Y. Wan, S. Li, and J. Liu, "High-sensitivity sensing based on intensity-interrogated bloch surface wave sensors," *Sensors and Actuators B: Chemical*, vol. 193, pp. 467–471, 2014.

[28] W. Yang, S. Song, X. Yi, S. X. Chew, L. Li, and L. Nguyen, "Silicon-on-insulator microring resonator sensor based on an amplitude comparison sensing function," *Optics Letters*, vol. 43, no. 1, pp. 70–73, 2017.

[29] Q. Wang, B.-T. Wang, L.-X. Kong, and Y. Zhao, "Comparative analyses of bi-tapered fiber mach–zehnder interferometer for refractive index sensing," *IEEE Transactions on Instrumentation and Measurement*, vol. 66, no. 9, pp. 2483–2489, 2017.

[30] R. Dersch, M. Steinhart, U. Boudriot, A. Greiner, and J. H. Wendorff, "Nanoprocessing of polymers: applications in medicine, sensors, catalysis, photonics," *Polymers for Advanced Technologies*, vol. 16, no. 2-3, pp. 276–282, 2005.

[31] T. Weil, T. Vosch, J. Hofkens, K. Peneva, and K. Müllen, "The rylene colorant family—tailored nanoemitters for photonics research and applications," *Angewandte Chemie International Edition*, vol. 49, no. 48, pp. 9068–9093, 2010.

[32] M. Moharam, E. B. Grann, D. A. Pommet, and T. Gaylord, "Formulation for stable and efficient implementation of the rigorous coupled-wave analysis of binary gratings," *JOSA a*, vol. 12, no. 5, pp. 1068–1076, 1995.

[33] T. Hemati and B. Weng, "Theoretical design of coupled high contrast grating (chcg) waveguides to enhance co2 light-absorption for gas sensing applications," *Journal of Applied Physics*, vol. 125, no. 15, 2019.

[34] U. D. Zeitner, M. Oliva, F. Fuchs, D. Michaelis, T. Benkenstein, T. Harzendorf, and E.-B. Kley, "High performance diffraction gratings made by e-beam lithography," *Applied Physics A*, vol. 109, pp. 789–796, 2012.

[35] B. C. Kress and P. Meyrueis, *Applied digital optics: from micro-optics to nanophotonics*. John Wiley & Sons, 2009.

[36] E. G. Loewen and E. Popov, *Diffraction gratings and applications*. CRC Press, 2018.

[37] L. Shamsuddin, K. Mohamed, and A. R. Maryam, "The investigation of microstructures fabrication on quartz substrate employing electron beam lithography (ebl) and icp-rie process," *Advanced Materials Research*, vol. 980, pp. 69–73, 2014.

[38] S. H. Oh, J. G. Kim, C. S. Kim, D. S. Choi, S. Chang, and M. Y. Jeong, "The fabrication of 3-d nanostructures by a low-voltage ebl," *Applied Surface Science*, vol. 257, no. 9, pp. 3817–3823, 2011.

[39] M. Åstrand, T. Frisk, H. Ohlin, and U. Vogt, "Understanding dose correction for high-resolution 50 kv electron-beam lithography on thick resist layers," *Micro and Nano Engineering*, vol. 16, p. 100141, 2022.